PCCP

Electron Nuclear Dynamics of Time-Dependent Symmetry Breakings in $H^+ + H_2O$ at E_{Lab} = 28.5–200.0 eV: A Prototype for Ion Cancer Therapy Reactions

Journal:	*Physical Chemistry Chemical Physics*
Manuscript ID	CP-ART-10-2022-004854.R1
Article Type:	Paper
Date Submitted by the Author:	27-Nov-2022
Complete List of Authors:	Dominguez, Juan; Texas Tech University, Chemistry and Biochemistry Kim, Hyunsik; Texas Technical University, Chemistry and Biochemistry Silva, Eivson; Texas Tech University, Chemistry and Biochemistry Pimbi, Daniel; Texas Tech University, Electrical and Computer Engineering Morales, Jorge; Texas Tech University, Chemistry and Biochemistry

SCHOLARONE™
Manuscripts

Electron Nuclear Dynamics of Time-Dependent Symmetry Breakings in $H^+ + H_2O$ at E_{Lab} = 28.5–200.0 eV: A Prototype for Ion Cancer Therapy Reactions

Juan C. Domínguez[1], Hyunsik Kim[1], Eivson D. Silva[1++], Daniel Pimbi[2], and Jorge A. Morales[1*]

[1]*Department of Chemistry and Biochemistry, Texas Tech University, Box 41061, Lubbock, TX 79409-1061, USA.*

[2]*Department of Electrical and Computer Engineering, Texas Tech University, Box 43102, Lubbock, TX 79409, USA*

*Corresponding author; *e -mail address*: jorge.morales@ttu.edu

++ Permanent Address: Department of Fundamental Chemistry, Federal University of Pernambuco, Recife, Pernambuco Brazil.

Abstract

Following our preceding research [PCCP, **21**, 5006, (2019)], we present an electron nuclear dynamics (END) investigation of $H^+ + H_2O$ at E_{Lab} = 28.5 – 200.0 eV in conjunction with a computational procedure to induce symmetry breaking during evolution. The investigated system is a computationally feasible prototype to simulate water radiolysis reactions in ion cancer therapy. END is a time-dependent, variational, non-adiabatic, and on-the-fly method, which utilizes classical mechanics for nuclei and a Thouless single-determinantal state for electrons. In this study, a procedure inherent to END introduces low degrees of symmetry breaking into the reactants' restricted Hartree-Fock (RHF) state to induce a higher symmetry breaking during evolution. Specifically, the Thouless exponential operator acting on the RHF reference generates an axial spin density wave (ASDW) state according to Fukutome's analysis of

HF symmetry breakings; this state exhibits spatial and spin symmetry breakings. By varying a Thouless parameter, low degrees of symmetry breaking are introduced into ASDW states. After starting the dynamics from those states, higher degrees of symmetry breaking may subsequently emerge as dictated by the END equations without *ad-hoc* interventions. Simulations starting from symmetry-conforming states preserve the symmetry features during dynamics, whereas simulations starting from symmetry-broken states display an upsurge of symmetry breaking once the reactants collide. Present simulations predict three types of reactions: (**I**) Projectile scattering, (**II**) hydrogen substitution, and (**III**) water radiolysis into H + OH and 2H + O fragments. Remarkably, symmetry breaking considerably increases the extent of the target-to-projectile electron transfers (ETs) occurring during the above reactions. Then, with symmetry breaking, 1-ET differential and integral cross sections increase in value, whereas 0-ET differential cross sections and primary rainbow scattering angles decrease. More importantly, END properties calculated from symmetry-breaking simulations exhibit better agreements with the experimental data. Notably, END 1-ET integral cross sections with symmetry breaking compare better with their experimental counterparts than 1-ET integral cross from high-level close-coupling calculations; moreover, END validates an undetected rainbow scattering peak inferred from the experimental data. A discussion of our symmetry-breaking procedure in the context of Fukutome's analysis of HF symmetry breakings is also presented.

Keywords: Symmetry breaking, electron nuclear dynamics, Thouless single-determinantal state, ion cancer therapy, electron transfer.

1. Introduction

It is well known in time-independent quantum chemistry that symmetry conditions satisfied by a restricted Hartree-Fock (RHF) wavefunction at equilibrium geometry can become into detrimental constraints at other geometries[1-3]. The dissociation of the H_2 molecule offers the simplest illustration of such a phenomenon. At equilibrium geometry, the RHF wavefunction of H_2 provides the minimum HF energy of this molecule and satisfies its spatial and spin symmetries. Specifically, H_2 exhibits a $D_{\infty h}$ spatial symmetry at all bond lengths; thus, its RHF spin-orbitals and RHF wavefunction corresponds to irreducible representations of the $D_{\infty h}$ group[1-3]. For instance, the highest occupied and lowest unoccupied molecular orbitals (HOMO and LUMO, respectively) span the 1-D irreducible representations σ_g and σ_u of $D_{\infty h}$, respectively. In addition, the RHF wavefunction of H_2 satisfies spin symmetry conditions[1] (i.e., spin adaptation[3]) by being an eigenfunction of the squared total and z-axis spin operators, $\hat{S}^2_{Total}$ and $\hat{S}_z$, with quantum numbers $S = 0$ and $M_S = 0$, respectively (a closed-shell singlet state)[1-3]. At large bond lengths, the RHF wavefunction of H_2 also satisfies the aforesaid symmetry conditions. However, due to the spatial symmetry constraints on the spin-orbitals, the asymptotic RHF wavefunction of H_2 is a superposition of states that describe a covalent dissociation into neutral atoms: $H_2 \rightarrow H + H$, and two ionic ones: $H_2 \rightarrow H^+ + H^-$ and $\rightarrow H^- + H^+$ [1-3]. In contrast, the gas-phase dissociation of H_2 at the ground state only produces neutral atoms. This unphysical RHF dissociation renders an overestimated dissociation energy that leads to incorrect predictions of bond making/breaking processes[1-3]. This inaccurate energetics reflects the fact that the RHF wavefunction does not provide the minimum HF energy of H_2 at large bond lengths[1-3].

A way to repair the RHF dissociation without abandoning a single-determinantal representation is to switch from a RHF wavefunction to an unrestricted HF (UHF) one at the dissociation limit[1-3]. By design,

a UHF wavefunction can violate some symmetry conditions at large bond lengths, and, therefore, provide the minimum HF energy, a dissociation into neutral atoms, and a reasonable dissociation energy. Unlike its RHF counterpart, a UHF wavefunction does not constraint any pair of α and β spin-orbitals to have the same spatial orbital. This flexibility to construct spin-orbitals allows the emergence of spatial and spin symmetry breakings. Regarding spatial symmetry, the UHF spin-orbitals at dissociation are linear combinations of RHF spin-orbitals belonging to different irreducible representations of the spatial symmetry group[1-3]; thus, in the dissociation limit, the UHF spin-orbitals and wavefunction do not comply with spatial symmetry conditions. For instance, in a dissociating H_2 with a minimal basis set, the two UHF spin-orbitals contain linear combinations of the RHF HOMO and LUMO belonging to the irreducible representations σ_g and σ_u of $D_{\infty h}$, respectively[1-3]. Thanks to this mixing of RHF orbitals, the UHF wavefunction can describe a dissociation into neutral atoms at large bond lengths. Regarding spin symmetry, a UHF wavefunction at dissociation is a superposition of spin eigenfunctions with different eigenvalues S and with the same eigenvalue M_S; therefore, this UHF wavefunction is an eigenfunction of $\hat{S}_z$ but not of $\hat{S}^2_{Total}$ [1-3]. This mixing of the correct spin eigenfunction with others is referred as spin contamination; it manifests in a non-integer squared total spin operator average $\left\langle \hat{S}^2_{Total} \right\rangle \neq S(S+1)$ for any total spin eigenvalue S. For instance, in a dissociating H_2 with a minimal basis set, the UHF wavefunction is a superposition of singlet ($S=0$) and triplet ($S=1$) spin eigenfunctions all with $M_S = 0$ [1-3]. The spatial and spin symmetry breaking in UHF at large bond lengths produces a spin density $\rho_s(\mathbf{r})$ that is not equal to zero at all points $\mathbf{r}$ [the RHF $\rho_s(\mathbf{r})$ for a closed-shell singlet state is zero everywhere]. For instance, the UHF $\rho_s(\mathbf{r})$ can develop positive values on one atom and negative values on another one as these two atoms undergo a bond breaking; this is an example of spin polarization. Spin contamination and spin

polarization quantified by $\left\langle \hat{S}^2_{Total} \right\rangle$ and $\rho_s(\mathbf{r})$, respectively, are useful indicators of symmetry breakings in single-determinantal wavefunctions.

The explained symmetry traits are not exclusive of the HF method: Any other method relying on a single-determinantal representation will exhibit similar patterns. Thus, the Kohn-Sham density functional theory (KSDFT) method, which represents the electron density with an auxiliary single-determinantal wavefunction, exhibits analogous symmetry-breaking characteristics[4]. Of course, one can obtain a correct dissociation description without violating symmetry conditions by using a multi-configuration method[2]; however, such an option may be computationally expensive. Thus, when computing large molecules with feasible HF or KSDFT, symmetry-broken wavefunctions are inevitable if one wants to describe correct dissociations[1].

In a ground-breaking publication[1], Fukutome demonstrated that there are eight possible ways to break symmetries in a single-determinantal state that correspond to eight types of symmetry-broken HF wavefunctions. Fukutome's analysis focused on spin and time reversal symmetries that can also involve spatial symmetries[1]. The eight symmetry-broken HF wavefunctions are categorized according to the symmetries that they still preserve despite the violation of others[1]. For instance, the previously discussed UHF wavefunction of H_2 is an example of the axial spin density wave (ASDW) wavefunction in Fukutome classification[1]. The ASDW wavefunctions are invariant under a spin rotation around a fixed axis (thus, a quantum number M_S is defined) and under a "magnetic" operation (the latter is the product of a spin rotation and a time reversal that generates a two-element discrete group[1]); however, the ASDW wavefunctions violate spatial and S-related spin symmetries as previously illustrated with the UHF wavefunction of H_2. Thus, the symmetry-broken ASDW states can describe proper HF dissociations of various molecules in the time-independent framework[1].

A key element in Fukutome' analysis[1] of HF symmetry breakings is the use of the Thouless representation of a single-determinantal state[5]. This representation permits the construction of the most

general single-determinantal states from a reference state and, hence, the development of all possible types of symmetry breakings. Specifically, Fukutome' analysis[1] takes a symmetry-complying RHF state as a reference state and applies to it the Thouless exponential operator in terms of complex-valued parameters[5]; by varying those parameters, all types of symmetry-broken single-determinantal states can be generated (cf. Sect. 2 and 3.3 for mathematical details)[1].

An elegant way to generate symmetry-broken HF or KSDFT wavefunctions in the time-independent framework is to employ the Thouless representation as described above. Alternatively, one can generate those symmetry-broken wavefunctions through their unrestricted self-consistent-field (SCF) procedures started from a symmetry-broken guess[1, 3]. Occasionally, those SCF procedures can get trapped in a RHF solution and fail to provide a symmetry-broken wavefunction[1, 3]; if so, restarting them from another symmetry-broken guess may lead to a broken-symmetry solution. This time-independent SCF treatment of symmetry breaking is easy to transfer to time-dependent dynamical methods based on potential energy surfaces (PESs). Specifically, the predetermined HF or KSDFT PESs can include appropriate symmetry-broken regions that drive the dynamics to correct reactions' descriptions. However, the situation is more complex in the case of direct dynamics methods that calculate on-the-fly wavefunctions and interaction potentials. In this case, symmetry-broken regions cannot be built a priori, and the time-dependent algorithms need to determine on-the-fly whether a symmetry breaking may emerge or not. The on-the-fly evaluation of a UHF wavefunction does not necessarily guarantee the emergence of symmetry breakings because, as happens with the time-independent SCF procedure, a time-dependent algorithm can get trapped in a symmetry-conforming RHF description[6]. A possible solution to this problem is to develop subroutines that check if symmetry breaking is advantageous at each time step of a simulation and enforce it if so. However, this solution involves various inconveniences, such as the extra computational cost to check and enforce symmetry breakings and the appropriate way to enforce it without spoiling the dynamics. More fundamentally, this solution defeats the purpose of a direct dynamics, wherein one

expects that the evolution of a system will automatically proceed from its initial conditions without on-the-fly interventions.

To overcome these problems, we devised a novel computational procedure to induce symmetry breakings in time-dependent direct dynamics without on-the-fly interventions[6]; we developed that procedure in the framework of the electron nuclear dynamics (END) method[7-9]. END is a time-dependent, variational, non-adiabatic, and direct method to simulate chemical reactions. In the simplest-level (SL) END (SLEND) version adopted herein[7-9], nuclei are described with classical mechanics, and electrons are represented with a single-determinantal wavefunction in the Thouless representation[5]. The SLEND dynamical equations are obtained through the time-dependent variational principle (TDVP)[10] that extends the use of the time-independent variational principle of HF to the time-dependent realm. In the original SLEND formulation[7-9], the role of the Thouless representation is to provide the most general single-determinantal state for the TDVP optimization. However, given its role in Fukutome analysis[1], we extended the use of the Thouless representation to induce time-dependent symmetry breakings in SLEND simulations. In this way, we innovatively started the extension of Fukutome's time-independent analysis of symmetry breaking to the time-dependent realm. In SLEND simulations, we usually start with the reactants at their equilibrium geometries, so they are properly described with a symmetry-conforming RHF wavefunction at initial time. As a SLEND simulation evolves, we usually observed that, despite using the unrestricted form of SLEND, the evolving electronic wavefunction can get trapped in a restricted solution that preserves the initial symmetries; this type of evolution finally leads to less accurate descriptions of dissociations and electron transfer (ET) processes[6, 11-13]. However, we also observed that if a small degree of symmetry breaking is introduced into the initial RHF wavefunction, this evolves in a nearly restricted and symmetry-conforming form for a while, but changes into an unrestricted and symmetry-broken form once the reactants collide[6, 11-13]. Like with the time-independent variational principle of HF, this time-dependent RHF-UHF transition happens if the TDVP favors a symmetry-broken

solution sometime during evolution[6, 11]. This symmetry breaking in the initial state can be seen as a small perturbation or as a small "seed" that predisposes the dynamical equations for a complete symmetry breaking at a later time. This symmetry-breaking "seed" in the time-dependent SLEND is analogous to the previously mentioned symmetry-broken guess in a SCF UHF calculation.

Following Fukutome[1], we generate the initial symmetry-broken states for SLEND simulations by applying the Thouless exponential operator to the symmetry-conforming RHF wavefunction of the reactants[6]. By varying the operator parameters, we can introduce small degrees of symmetry breaking into the RHF reference state and transform it into a symmetry-broken ASDW state[1] from which the dynamics starts. We successfully applied this procedure to SLEND simulations of $H^+ + C_2H_4$ at E_{Lab} = 30 eV[6]. A main result from that study is that symmetry breaking considerably increases the extent of target-to-projectile ET processes as revealed by various properties, such as Mulliken populations, ET probabilities and 1-ET integral cross sections (ICSs)[6]. More importantly, results from symmetry-breaking simulations agreed much better with the available experimental data than results from their symmetry-conforming counterparts[6]. Remarkably, only the 0- and 1-ET differential cross sections (DCSs) from symmetry-breaking simulations agreed with the experimental data (e.g., only the symmetry-breaking simulations predicted the experimentally observed order 1-ET DCS > 0-ET DCS at all scattering angles; the symmetry-conforming simulations incorrectly predict the inverse order)[6]. We found similar improvements in SLEND results via symmetry breaking in $H^+ + N_2O$[11], $+ CO_2$[11], $+ H_2O$[12], and $+ C_2H_2$.

In this publication, we will further apply our symmetry-breaking procedure to SLEND simulations of $H^+ + H_2O$ at E_{Lab} = 28.5 – 200.0 eV[14-17]. This system is particularly important because it constitutes a computationally feasible prototype to simulate ion cancer therapy (ICT) reactions with quantum dynamics methods[18-20]. ICT utilizes high-energy ion projectiles (e.g., H^+ and C^{6+}) to obliterate cancerous tumors with minimum damage to healthy tissues[18-20]. Basically, in ICT, the ion projectiles predominantly collide with the H_2O molecules of a patient body to trigger water radiolysis reactions. Those reactions produce

various secondary particles (ions, radicals, and reactive molecules) that ultimately damage the DNA of cancerous cells. We successfully applied SLEND to simulate various types of ICT reactions in systems involving H_2O, DNA/RNA bases, and DNA nucleotides[8, 21-26]. For instance, we investigated $H^+ + (H_2O)_n$ for $n = 3-4$ at E_{Lab}=1 keV[22, 24] and for $n = 1-6$ at E_{Lab}=100 keV[23, 24] to predict reactive processes and 1-ET ICSs. Herein, we study again $H^+ + H_2O$, but we consider new conditions, properties, and phenomena. Specifically: **(1)** we explore a new energy range E_{Lab} = 28.5 – 200.0 eV; **(2)** we predict 1-ET DCSs and other properties in addition to reactive processes and 1-ET ICSs; and **(3)** we investigate the effect of symmetry breaking on these reactions for the first time. Therefore, this study has the double purpose of further investigating time-dependent symmetry breakings in chemical reactions and of elucidating microscopic details of water radiolysis in ICT.

2. Method:

Our symmetry-breaking procedure is associated with the SLEND method[7-9]; therefore, we will briefly outline SLEND to understand such a procedure. SLEND is a time-dependent, variational, non-adiabatic, and direct method to simulate chemical reactions. SLEND adopts a total trial wavefunction $\left|\Psi_{Total}^{SLEND}\right\rangle = \left|\Psi_{N}^{SLEND}\right\rangle \left|\Psi_{e}^{SLEND}\right\rangle$ that is the product of nuclear $\left|\Psi_{N}^{END}\right\rangle$ and electronic $\left|\Psi_{e}^{END}\right\rangle$ wavefunctions. $\left|\Psi_{N}^{SLEND}\right\rangle$ is the product of N_N frozen Gaussian wave packets representing the N_N nuclei of a system:

$$\left\langle \mathbf{X}\middle|\Psi_{N}^{SLEND}(t)\right\rangle = \left\langle \mathbf{X}\middle|\mathbf{R}(t),\,\mathbf{P}(t)\right\rangle = \prod_{A=1}^{3N_N}\exp\left\{-\left[\frac{X_A - R_A(t)}{2\Delta R_A}\right]^2 + iP_A(t)\left[X_A - R_A(t)\right]\right\}; \qquad (1)$$

where $\mathbf{R}_A(t)$, $\mathbf{P}_A(t)$ and ΔR_A are the wave packets' positions, momenta, and widths, respectively. The wave packets are employed in the zero-width limit, a procedure that renders a classical nuclear dynamic in terms of $\mathbf{R}_A(t)$ and $\mathbf{P}_A(t)$. $\left|\Psi_{e}^{SLEND}\right\rangle$ is a spin-unrestricted, single-determinantal wavefunction in the

Thouless representation[5]. In a system with N_e electron and with a basis set of size $K > N_e$, $\left|\Psi_e^{SLEND}\right\rangle$ is constructed in terms of N_e occupied (hole) $\{\psi_h\}$ and $K - N_e$ unoccupied (particle) $\{\psi_p\}$ HF molecular spin-orbitals (MSOs):

$$\begin{aligned}\left|\Psi_e^{SLEND}\right\rangle &= \exp\left[\sum_{h=1,\, p=N_e+1}^{N_e,\, K} z_{ph}(t)\, b_p^\dagger b_h\right]\left|0\right\rangle = \left|\chi_1 \cdots \chi_h \cdots \chi_{N_e}\right\rangle; \\ &= \left|0\right\rangle + \sum_{p,h} z_{ph}(t)\, b_p^\dagger b_h \left|0\right\rangle + \sum_{p,\,h,\,p',h'} b_p^\dagger b_{p'}^\dagger b_{h'} b_h \left|0\right\rangle + \ldots;\end{aligned} \qquad (2)$$

where $\left|\mathbf{O}\right\rangle = \left|\psi_1 \ldots \psi_h \ldots \psi_{N_e}\right\rangle$ is a HF reference state, and the $\{\chi_h\}$ are unrestricted dynamical spin-orbitals (DSOs):

$$\chi_h\left[\mathbf{x};\, \mathbf{R}(t), \mathbf{P}(t)\right] = \psi_h\left[\mathbf{x};\, \mathbf{R}(t), \mathbf{P}(t)\right] + \sum_{p=N_e+1}^{K} z_{ph}(t)\, \psi_p\left[\mathbf{x};\, \mathbf{R}(t), \mathbf{P}(t)\right];\ (1 \le h \le N_e); \qquad (3)$$

with complex-valued coefficients $\{z_{ph}(t)\}$. Each χ_h is a linear combination of one occupied (hole) MSO ψ_h with all the unoccupied (particle) MSOs $\{\psi_p\}$ [1, 5]. The HF MSOs are constructed with travelling atomic basis set functions centered on the moving nuclei. Eq. (2) shows the effects of the Thouless exponential operator with particle-hole pairs operators $\{b_p^\dagger b_h\}$ on the ground state $\left|0\right\rangle$: **(1)** To transform the reference HF MSOs $\{\psi_h\}$ into the DSOs $\{\chi_h\}$ [5], and **(2)** to express $\left|\Psi_e^{SLEND}\right\rangle$ as a superposition of the ground state $\left|0\right\rangle$ and all its singly, doubly, etc., excited states; the latter reveals the non-adiabatic nature of SLEND (cf. Refs. [7, 8] for more details). In addition to these effects, the Thouless representation provides an ingenious way to prepare symmetry-broken states at initial time, a procedure that links SLEND with the Fukutome's analysis of symmetry breakings (cf. Refs [1, 6] and Sect. 3 below). The SLEND dynamical equations are obtained by applying the TDVP[10] to $\left|\Psi_{Total}^{SLEND}\right\rangle$:

$$\begin{bmatrix} i\mathbf{C} & \mathbf{0} & i\mathbf{C}_{\mathbf{R}} & i\mathbf{C}_{\mathbf{P}} \\ \mathbf{0} & -i\mathbf{C}^{*} & -i\mathbf{C}_{\mathbf{R}}^{*} & -i\mathbf{C}_{\mathbf{P}}^{*} \\ i\mathbf{C}_{\mathbf{R}}^{\dagger} & -i\mathbf{C}_{\mathbf{R}}^{T} & \mathbf{C}_{\mathbf{RR}} & -\mathbf{I}+\mathbf{C}_{\mathbf{RP}} \\ i\mathbf{C}_{\mathbf{P}}^{\dagger} & -i\mathbf{C}_{\mathbf{P}}^{T} & \mathbf{I}+\mathbf{C}_{\mathbf{PR}} & \mathbf{C}_{\mathbf{RP}} \end{bmatrix} \begin{bmatrix} \frac{d\mathbf{z}}{dt} \\ \frac{d\mathbf{z}^{*}}{dt} \\ \frac{d\mathbf{R}}{dt} \\ \frac{d\mathbf{P}}{dt} \end{bmatrix} = \begin{bmatrix} \frac{\partial E_{Total}}{\partial \mathbf{z}^{*}} \\ \frac{\partial E_{Total}}{\partial \mathbf{z}} \\ \frac{\partial E_{Total}}{\partial \mathbf{R}} \\ \frac{\partial E_{Total}}{\partial \mathbf{P}} \end{bmatrix}. \quad (4)$$

Above, $E_{Total} = E_{Total}\left[\mathbf{R}(t), \mathbf{P}(t), \mathbf{z}(t), \mathbf{z}^{*}(t)\right]$ is the total energy, and $i\mathbf{C}$, $i\mathbf{C}_{\mathbf{R}}$, $\mathbf{C}_{\mathbf{RP}}$, etc., are the dynamic metric matrices[7-9]; $i\mathbf{C}_{\mathbf{R}}$ and $\mathbf{C}_{\mathbf{RR}}$ bear similarity to the standard non-adiabatic coupling terms[27, 28].

3. Computational Details

3.1 Preparation of the Initial Conditions Common to Symmetry-Preserving and Symmetry-Breaking Simulations.

The computational protocol to prepare and run symmetry-preserving and symmetry-breaking SLEND simulations was explained in detail in our Ref. [6]. Therefore, herein, we will explain that protocol applied to $H^+ + H_2O$ in an abbreviated form; the reader can find further information in Ref. [6]. The preparation of SLEND simulations with and without initial symmetry breaking are identical, except that when we seek the former effect, we perform an additional step to incorporate a low degree of symmetry breaking in the initial wavefunction. Then, in this section, we will describe the preparation of the initial conditions common to symmetry-preserving and symmetry-breaking simulations; we will describe the additional step to set up symmetry-breaking simulations in the following section.

The initial conditions of the H^+ and H_2O reactants are shown in Fig. 1. The H_2O target is prepared at rest in its ground-state equilibrium geometry at the RHF level with the 6-31G** basis set because a restricted solution provides the global HF energy minimum at this configuration; however, we will perform all the subsequent dynamics with the unrestricted form of SLEND to allow the emergence of symmetry breakings. The center of mass of the H_2O target is placed at the origin of the laboratory-frame

coordinate axes. The ground-state equilibrium geometry of H_2O has C_{2v} spatial symmetry. Then, H_2O is placed with its molecular plane on the *y-z* plane of the coordinate system and with its symmetry axis $\hat{C}_2$ placed along the *z*-axis. The H^+ projectile is first prepared with position $\mathbf{R}_{H^+}^{(0)} = (b \geq 0,\ 0,\ +30 \text{ a.u.})$ and momentum $\mathbf{P}_{H^+}^{(0)} = (0, 0, -p_{H^+}^z)$, where $b \geq 0$ is the projectile impact parameter from the H_2O center of mass, and $p_{H^+}^z$ corresponds to one of the six collision energies selected for this study: $E_{Lab} = 28.5,\ 48.6,$ 50.0, 70.0, 100.0, and 200.0 eV. The definite initial conditions $\mathbf{R}_{H^+}^{(i)}$ and $\mathbf{P}_{H^+}^{(i)}$ of H^+ are obtained by rotating $\mathbf{R}_{H^+}^{(0)}$ and $\mathbf{P}_{H^+}^{(0)}$ through the extrinsic Euler angles[29]: $0^0 \leq \gamma < 360^0$, $0^0 \leq \beta \leq 180^0$, and $0^0 \leq \alpha < 360^0$, around the space-fixed *z, y*, and *z* axes, respectively[29]. These rotations generate relative projectile-target orientations $\omega_i = (\alpha_i, \beta_i, \gamma_i)$; the ω_i are selected from a 120-point grid: $1 \leq i \leq 120$, = twice the 60-point uniform grid of Ref. [30]. However, thanks to the C_{2v} symmetry of H_2O, only 34 non-equivalent orientations ω_i out of a total of 120 are needed for these simulations. For each ω_i, b is varied from b = 0.0 a.u. to 9.0 a.u in steps of $\Delta b = 0.1$ a.u., and from b = 9.0 a.u. to 12.5 a.u. in steps of $\Delta b = 0.5$ a.u. For each energy, we perform two sets of simulations: **(1)** a set without initial symmetry breaking, and **(2)** another set with a low degree of initial symmetry breaking. Each set of simulations for a given energy comprises 3,332 non-equivalent trajectories; the whole study, with two sets of simulations at six energies, comprises 39,984 non-equivalent trajectories. All simulations run for a total time of 1,750 a.u. (42.3325 fs), which is long enough to obtain a final projectile-target separation that is at least equal to the initial one.

3.2 Preparation of the Additional Initial Conditions for Symmetry-Breaking Simulations.

As discussed in the Introduction, we employ Fukutome's ASDW state $|\overline{0}\rangle_{ASDW}$ [1, 6] as the appropriate symmetry-broken state at initial time. We generate $|\overline{0}\rangle_{ASDW}$ by applying the Thouless exponential operator[5] to the symmetry-conforming RHF state $|0\rangle$ describing the reactants[1, 6]. At initial time, our system

consists of an electron-stripped H^+ projectile well-separated from the H_2O target; then, the initial $|0\rangle$ and $|\overline{0}\rangle_{ASDW}$ are based on the H_2O molecule. In principle, all the occupied RHF MSOs of H_2O can be affected by symmetry breaking[1]. However, as demonstrated in Ref.[6], it suffices to introduce the initial symmetry breaking into the frontier MSOs of $|0\rangle = |\psi_1^\alpha \psi_1^\beta ... \psi_4^\alpha \psi_4^\beta \psi_{HOMSO}^\alpha \psi_{HOMSO}^\beta\rangle = |[...]\psi_{HOMSO}^\alpha \psi_{HOMSO}^\beta\rangle$, where ψ_{HOMSO}^α and ψ_{HOMSO}^β are the α - and β-spin RHF highest occupied MSOs (HOMOSs), whose symmetries will be broken at initial time, and $\psi_1^\alpha \psi_1^\beta ... \psi_4^\alpha \psi_4^\beta = [...]$ are the rest of the RHF MSOs, whose symmetries will be preserved at initial time. The Thouless exponential operator to generate $|\overline{0}\rangle_{ASDW}$ from $|0\rangle$ only includes the particle-hole pairs operators $b_{LUMSO}^{\alpha/\beta\dagger} b_{HOMSO}^{\alpha/\beta}$ [cf. Eq. (2)] with Thouless parameters $z_{LUMSO,\,HOMSO}^\alpha = -z_{LUMSO,\,HOMSO}^\beta = \tan\phi$, where ϕ, $0^0 \le \phi < 360^0$, is our symmetry breaking parameter[6]. Then, the normalized ASDW state $|\overline{0}\rangle_{ASDW}$ is[6] [cf. Eqs. (2) and (3)]

$$\begin{aligned} |\overline{0}\rangle_{ASDW}(\phi) &= \cos^2\phi \, \exp\left(z_{LUMSO,\,HOMSO}^\alpha b_{LUMSO}^{\alpha\dagger} b_{HOMSO}^\alpha + z_{LUMSO,\,HOMSO}^\beta b_{LUMSO}^{\beta\dagger} b_{HOMSO}^\beta\right)|0\rangle \\ &= \cos^2\phi \, \exp\left[\tan(\phi) b_{LUMSO}^{\alpha\dagger} b_{HOMSO}^\alpha - \tan(\phi) b_{LUMSO}^{\beta\dagger} b_{HOMSO}^\beta\right]|[...]\psi_{HOMSO}^\alpha \psi_{HOMSO}^\beta\rangle \\ &= |[...](\cos\phi\varphi_{HOMO} + \sin\phi\varphi_{LUMO})\alpha(\cos\phi\varphi_{HOMO} - \sin\phi\varphi_{LUMO})\beta\rangle = |[...]\psi_{HOMSO}^{SB\,\alpha}\psi_{HOMSO}^{SB\,\beta}\rangle; \end{aligned} \quad (5)$$

where the symmetry-broken HOMSOs $\psi_{HOMSO}^{SB\,\alpha/\beta}$ violate spatial symmetry as they combine the HOMO φ_{HOMO} and LUMO φ_{LUMO} belonging to the irreducible representations b_2 and a_1 of C_{2v}, respectively. Then, by changing the value of ϕ in Eq. (5), we can introduce different degrees of symmetry breaking into the $\psi_{HOMSO}^{SB\,\alpha/\beta}$ and $|\overline{0}(\phi)\rangle_{ASDW}$[6]; $\phi = 0^0$ corresponds to a symmetry-conforming situation. To reveal the spin symmetry breaking, $|\overline{0}(\phi)\rangle_{ASDW}$ can also be expressed as [6] (cf. Eq. (2), third line):

$$\begin{aligned}\left|\overline{0}(\phi)\right\rangle_{ASDW} &= \cos^2\phi\left|[...]\psi^{\alpha}_{HOMSO}\ \psi^{\beta}_{HOMSO}\right\rangle - \sin^2\phi\left|[...]\psi^{\alpha}_{LUMSO}\ \psi^{\beta}_{LUMSO}\right\rangle \\ &\quad - 2^{1/2}\cos\phi\sin\phi\frac{1}{2^{1/2}}\left[\left|[...]\psi^{\alpha}_{HOMSO}\ \psi^{\beta}_{LUMSO}\right\rangle - \left|[...]\psi^{\alpha}_{LUMSO}\ \psi^{\beta}_{HOMSO}\right\rangle\right] \qquad (6) \\ &= \cos^2\phi\left|{}^1\Psi_0\right\rangle - \sin^2\phi\left|{}^1\Psi_1\right\rangle - 2^{1/2}\cos\phi\sin\phi\left|{}^3\Psi_1\right\rangle;\end{aligned}$$

where $\left|{}^1\Psi_0\right\rangle$ is the singlet RHF ground state, $\left|{}^1\Psi_1\right\rangle$ the first singlet RHF excited state, and $\left|{}^3\Psi_1\right\rangle$ the first triplet RHF excited state. Each of these states is an eigenfunction of $\hat{S}_z$ with eigenvalue $M_S = 0$, and so is $\left|\overline{0}(\phi)\right\rangle_{ASDW}$ for all values of ϕ. However, for most ϕ, $\left|\overline{0}(\phi)\right\rangle_{ASDW}$ is not an eigenfunction of $\hat{S}^2$ because it combines singlet and triplet states.

To illustrate the changes in the energy and spin symmetry of $\left|\overline{0}(\phi)\right\rangle_{ASDW}$ with respect to ϕ, Fig. 2 shows its relative HF/6-31G** energy $\Delta E_{HF}(\phi)$ with respect to the ground-state value, and its average squared total spin $\left\langle\hat{S}^2(\phi)\right\rangle$ vs. ϕ; these properties correspond to H_2O in its ground-state C_{2v} equilibrium geometry. In Fig. 2, the lowest $\Delta E_{HF}(\phi)$ values at ϕ = 0^0 and 180^0 correspond to the symmetry-conforming singlet RHF ground state $\left|{}^1\Psi_0\right\rangle$ with $\left\langle\hat{S}^2(\phi)\right\rangle = 0$ a.u., cf. Eq.(6); $\left|{}^1\Psi_0\right\rangle$ provides the global HF energy minimum. The highest $\Delta E_{HF}(\phi)$ value at ϕ = 90^0 corresponds to the symmetry-conforming first-excited singlet RHF state $\left|{}^1\Psi_1\right\rangle$ with $\left\langle\hat{S}^2(\phi)\right\rangle = 0$ a.u. All other values of ϕ correspond to $\left|\overline{0}(\phi)\right\rangle_{ASDW}$ that combine singlet and triplet states and has $\left\langle\hat{S}^2(\phi)\right\rangle \neq$ 0 or 2.

Our simulations correspond to $H^+ + H_2O$ experiments that utilized H_2O molecules in its singlet ground state[14-17]. Therefore, the degree of symmetry breaking introduced into a singlet ground-state H_2O molecule should be moderate to avoid an excessive distortion of the singlet ground-state character of H_2O. Therefore, in the present simulations, we will employ two values of ϕ listed in Table 1: $\phi_1 = 0^0$ and ϕ_2 =10.24157218^0, which correspond to null and low degrees of symmetry breaking, respectively. We

employ the selected value of ϕ_2 because it led to the best agreements with experimental data in various symmetry-breaking simulations[6, 11]. Table 1 also lists the values of $\langle \hat{S}^2(\phi) \rangle$ of $|\overline{0}(\phi)\rangle_{ASDW}$ of H_2O for ϕ_1 and ϕ_2 as a measure of the degree of symmetry breaking. We run SLEND simulations starting from the reference HF state $|0\rangle = |\overline{0}(\phi_1)\rangle_{ASDW}$ to investigate if symmetry breaking can develop during dynamics when departing from a symmetry-conforming state. In addition, we run SLEND simulations starting from $|0\rangle = |\overline{0}(\phi_2)\rangle_{ASDW}$ to investigate if a low initial symmetry breaking can induce a full symmetry breaking during dynamics. Unlike $|\overline{0}(\phi_1)\rangle_{ASDW}$, $|\overline{0}(\phi_2)\rangle_{ASDW}$ is not a fully optimized SCF HF state, but it is close to it because of the low value of ϕ_2 (cf. Fig. 2). Therefore, simulations from $\phi = \phi_2$ exhibit slight oscillations in the spin density before the reactants' collision. Those initial oscillations are negligible in comparison to those generated by the full symmetry breaking after the reactants' collision.

4. Results and discussion

4.1 Reactive Processes

Present SLEND/6-31G** simulations of $H^+ + H_2O$ at E_{Lab} = 28.5 – 200.0 eV predict three main types of chemical reactions. These three types of reactions occur in both symmetry-preserving and symmetry-breaking simulations; they are:

(I) Simple projectile scattering, where the incoming projectile H_p^+ scatters away as $H_p^{q_2}$ after capturing some electron density from H_2O; the latter species remains intact after the collision:

$$H_p^+ + H_2O \rightarrow H_2O^{q_1} + H_p^{q_2};\ q_1 + q_2 = +1 \quad \text{(I)}. \qquad (7)$$

In the above and subsequent chemical equations, the incoming projectile bears the subscript "p", H_p^+, in order to discern its final fate: either as a scattered projectile or as a nucleus combined into a product. In

addition, the q_i in the chemical equations denote the charges of the final species; these charges reflect electron-transfer processes occurring among the chemical species (cf. Sect. 4.2 for more details).

(II) Hydrogen substitution, where the incoming projectile H_p^+ substitutes one of the H atoms of H_2O:

$$H_p^+ + H_2O \rightarrow HOH_p^{q_1} + H^{q_2};\ q_1 + q_2 = +1 \quad \text{(II)}. \tag{8}$$

(III) Collision-induced water radiolysis into H + OH or 2H + OH fragments, where the collision of the incoming projectile H_p^+ produces H_2O fragmentations:

$$\begin{aligned} &H_p^+ + H_2O \rightarrow OH^{q_1} + H_p^{q_2} + H^{q_3}; && \sum_{i=1}^{3} q_i = +1 \quad \text{(IIIa)}; \\ &H_p^+ + H_2O \rightarrow O^{q1} + H_p^{q_2} + H^{q_3} + H^{q_4}; && \sum_{i=1}^{4} q_i = +1 \quad \text{(IIIb)}. \end{aligned} \tag{9}$$

The formation of the reactive species OH^{q_1} and O^{q_1} in the last two reactions is relevant for ICT because they are two important components of the secondary radiation that damages the DNA of cancerous cells[18-20]. In all the Reactions I-III, the final molecular species, $H_2O^{q_1}$ and OH^{q_1}, also undergo rotational, vibrational and electronic excitations in addition to the aforesaid electron transfers.

Reaction I is the predominant process in this system: it occurs for most of the values of the impact parameter b in the explored range: $0.0 \leq b \leq 12.5$ a.u., and becomes the sole process for high impact parameters $b \geq$ 5.0 a.u. (i.e., when the H_p^+ projectile approaches the H_2O target at a relatively long distance). The more involved Reactions II and III occur for some low impact parameters $b <$ 5.0 (i.e. when the H_p^+ projectile closely encounters the H_2O target). With only three main types of reactions, Eqs. (7)-(9), $H^+ + H_2O$ at E_{Lab} = 28.5 – 200.0 eV displays a less varied reactivity than $H^+ + C_2H_4$ at E_{Lab} = 30 eV, which displayed six main types of reactions with various subtypes within each of them[6].

To illustrate the predicted reactions and reveal time-dependent symmetry breakings, we show in Figs. 3-5 some sequential snapshots of three selected symmetry-breaking simulations ($\phi = \phi_2$) corresponding to Reactions I, II and III, respectively. To visualize the atoms motions, Figs. 3-5 represent the classical nuclei as colored spheres (red = O, white = H). In addition, to visualize symmetry breakings, Figs. 3-5 show colored clouds corresponding to isosurfaces of the spin density $\rho_s(\mathbf{r})$ (green and purple clouds that correspond to selected opposite values of that density: $\rho_s(\mathbf{r})$ and $-\rho_s(\mathbf{r})$, respectively). Additional information about the simulations in Figs. 3-5 can be found in their corresponding captions. To illustrate a reaction interpretation, we will briefly discuss the evolution details of the symmetry-breaking simulation in Fig. 4 that corresponds to Reaction II, hydrogen substitution. In the first frame of Fig. 4 (time = 0.0 fs.), we see the initial H_2O target before collision (the distant incoming projectile H_p^+ is off camera at this time). In the second frame (time = 19.35 fs), the incoming projectile H_p^+ approaches H_2O from the left. In these two frames, we can barely discern small and faint spin density clouds on H_2O that reveal its initial low spin symmetry breaking. In the third frame (time = 21.29 fs.), the incoming projectile H_p^+ gets close to one of the H atoms of H_2O and starts to bond to the O atom. In the four frame (time = 22.98 fs), the incoming projectile H_p^+ finally displaces the approached H atom into an upward-right direction and completely bonds to the O atom. At this point, the spin density clouds become somewhat more visible, a sign that spin breaking is increasing as a result of the close interactions between reactants. In the fifth frame (time = 26.61 fs), the displaced H atom moves further away from the new H_2O molecule formed by hydrogen substitution. At this point, the spin density clouds become even more visible and display different colors on each fragment: purple on H_2O and green on the H atom; this fact reveals an even increased degree of symmetry breaking, and the development of spin polarization between species that follow a UHF dissociation. Finally, in the sixth frame (time = 42.33 fs), we can see the final and isolated H_2O molecule.

Inspection of the last two frames reveals that the final H_2O molecule also undergoes rotational and vibrational motions. The way to interpret the symmetry-breaking simulations in Figs. 3 and 5 is similar to that of Fig. 4. In these three cases, and in all other symmetry-breaking simulations, the strong increase in symmetry breaking appears around the time of the closest approach of the reactants. To illustrate a case with no symmetry breaking, we show in Fig. 6 some sequential snapshots of a selected symmetry-preserving simulation ($\phi = \phi_1$) corresponding to Reaction I, simple projectile scattering. In this case, the spin density $\rho_s(\mathbf{r})$ remains equal to zero in all points of space during the whole simulation so that no isosurface clouds of $|\rho_s(\mathbf{r})| > 0$ appear; this reveals that the spin symmetry is preserved throughout the whole process. In lieu of the spin density, we show in Fig. 6 a selected isosurface of the total electron density $\rho_T(\mathbf{r})$ as red clouds; these clouds permit visualizing electron transfers between the reactants. Regarding the reaction itself in Fig 6, we see in its first frame (time = 0.0 fs) the initial H_2O target before collision displaying its total electron density cloud. In the second frame (time = 15.72 fs), the incoming projectile H_p^+ approaches H_2O from above. In the third frame (time = 19.35 fs), the H_p^+ projectile gets so close to H_2O that the total density cloud envelops both reactants; this indicates a transient electron transfer from H_2O to H_p^+. In the fourth frame (times = 22.98 fs), the projectile gets very close to the O atom and starts to deflect into the viewer's direction; in the following frame (time = 26.85 fs), the projectile finally scatters into the viewer's direction while capturing a small portion of electron density. Finally, in the sixth frame (time = 42.33 fs), we see the final and isolated H_2O molecule undergoing rotational and vibrational motions.

4.2 Electron-Transfer Reactions

An important subclass of reactions occurring in the investigated system are the target-to-projectile *n*-electron transfer (*n*-ET) reactions:

$$H_p^+ + H_2O \rightarrow H_p^{q_1=1-n} + \left(H_2O \text{ products}\right)^{q_2=n}, \quad n=0,\ 1,\ 2\ ... \quad (10)$$

The above ET reactions encompass all the predicted main reaction types I-III, Eqs. (7)-(9), which lead to outgoing projectiles $H_p^{q_1=1-n}$ and associated products, $\left(H_2O \text{ products}\right)^{q_2=n}$. These ET reactions can be quantified in terms of the total target-to-projectile *n*-ET ICSs, σ_{n-ET} [8]:

$$\sigma_{n-ET} = \frac{1}{4\pi}\int_0^{\infty}\int_0^{2\pi}\int_0^{\pi}\int_0^{2\pi} P_{n-ET}\left(\alpha,\beta,\gamma,b\right) b\sin\left(\beta\right) dbd\alpha d\beta d\gamma \ ; (11) \quad \text{where}$$

$P_{n-ET}\left(\alpha,\beta,\gamma,b\right)$ is the *n*-ET probability of a trajectory from projectile-target orientation $\left(\alpha,\beta,\gamma\right)$ and impact parameter b. Notice that in atom-atom collisions with spherically symmetric potentials, $P_{n-ET}\left(\alpha,\beta,\gamma,b\right) \rightarrow P_{n-ET}\left(b\right)$, and Eq. (11) transforms into the familiar expression $\sigma_{n-ET} = 2\pi \int_0^{\infty} P_{n-ET}\left(b\right) bdb$ [27]. The probability of forming hydrogen ions $H_p^{q_1=1-n}$ with $n \geq 3$ is negligible due to their high instability; then, in practice, the outgoing projectile $H_p^{q_1=1-n}$ can capture a maximum of two electrons. For such a situation, we demonstrated mathematically that the SLEND *n*-ET probabilities $P_{n-ET}\left(\alpha,\beta,\gamma,b\right)$ for $0 \leq n \leq 2$ from the final SLEND electronic wavefunction are[11, 26]

$$\begin{aligned} &P_{0-ET}\left(\alpha,\beta,\gamma,b\right) = \left(1-N_\alpha\right)\left(1-N_\beta\right); \\ &P_{1-ET}\left(\alpha,\beta,\gamma,b\right) = N_\alpha\left(1-N_\beta\right) + N_\beta\left(1-N_\alpha\right);\ P_{2-ET}\left(\alpha,\beta,\gamma,b\right) = N_\alpha N_\beta; \end{aligned} \quad (12)$$

where N_α and N_β are the Mulliken populations of the α- and β-spin electrons on the final outgoing projectile $H_p^{q_1=1-n}$. Eq. (12) is applied when the projectile is far away from all other fragments; thus, its Mulliken populations $N_{\alpha/\beta}$ are free of any subjective criteria to assign electrons to atoms and become exact as $N_{\alpha/\beta} = \int \rho_{\alpha/\beta}^{\text{Projectile}}\left(\mathbf{r}\right) d\mathbf{r}$, where $\rho_{\alpha/\beta}^{\text{Projectile}}$ is the α- or β-spin electron density of the isolated projectile.

Before discussing the *n*-ET ICSs, σ_{n-ET}, we will examine the symmetry-breaking effects on their components $N_{\alpha/\beta}$ and $P_{n-ET}(\alpha,\beta,\gamma,b)$, cf. Eqs. (11)-(12). Fig. 7 plots the α - and β -spin electron Mulliken populations of the all the nuclei at final time from SLEND/6-31G** simulations at E_{Lab} = 28.5 eV with initial projectile-target orientation $(0°, 0°, 0°)$, impact parameter b = 0.5 a.u., and symmetry-breaking parameters ϕ_1 (left panel) and ϕ_2 (right panel). These simulations correspond to Reaction I, simple projectile scattering, Eq. (7). In the symmetry-preserving dynamics (ϕ_1), the final outgoing projectile has identical α - and β -spin electron Mulliken populations: $N_\alpha(\phi_1) = N_\beta(\phi_1) = 0.028$; this equipartition of α and β Mulliken populations is also observed in the electron Mulliken populations of all the final target nuclei. These facts indicate that with ϕ_1 the system super-molecule finally separates as $(\mathbf{H}_p\text{---}\mathbf{H_2O})^+ \rightarrow \mathrm{H}_p^{q_1} + \mathrm{H_2O}^{q_2}$ via a symmetry-preserving RHF dissociation[1]. However, in the symmetry-breaking dynamics (ϕ_2), the final outgoing projectile does not have the same number of α - and β -spin electron Mulliken populations because $N_\alpha(\phi_2)$ = 0.017 ≠ $N_\beta(\phi_2)$ = 0.867. The α and β Mulliken populations of the final target nuclei also exhibit similar disproportions between them. Specifically, the disproportion is pronounced on the O atom and in the opposite way of that of $\mathrm{H}_p^{q_1}$, and is slight on the H atoms and in the same way as that of $\mathrm{H}_p^{q_1}$. These facts indicate that with ϕ_2 the system super-molecule finally separates via a symmetry-breaking UHF dissociation[1]. Remarkably, the total number of electrons transferred to the final projectile, $N_\alpha(\phi_i) + N_\beta(\phi_i)$, is 0.056 with ϕ_1 and 0.884 with ϕ_2, a fact that indicates that symmetry breaking favors ET reactions.

The symmetry-breaking effects on the ET probabilities are more enlightening. Fig. 8 plots the *n*-ET probabilities $P_{n-ET}(\alpha,\beta,\gamma,b)$ for $0 \le n \le 2$, Eq.(12), vs. the impact parameter b of SLEND/6-31G** simulations at E_{Lab} = 28.5 eV from orientation $(180^0,\ 180^0,\ 0^0)$ and with symmetry-breaking parameters ϕ_1

(left panel) and ϕ_2 (right panel). In the symmetry-preserving case, ϕ_1, we observe that $P_{0-ET} > P_{1-ET} >> P_{2-ET}$ for all b's; this result indicates that the 0-ET process always predominates over the 1- and 2-ET ones if symmetry breaking does not occur. In contrast, in the symmetry-breaking case, ϕ_2, we observe that $P_{1-ET} > P_{0-ET} >> P_{2-ET}$ for $0 \leq b \leq\approx 5.0$ a.u.; this result indicates that the 1-ET process predominates over the 0- and 2-ET ones in that impact parameter range if symmetry breaking occurs; the increase of the 1-ET probability over the 0-ET one by symmetry breaking is considerable. However, with ϕ_2, we observe that finally $P_{0-ET} > P_{1-ET} >> P_{2-ET}$ for $b >\approx 5.0$ a.u. despite symmetry breaking. This is expected because as b increases so does the projectile-target distance that gradually restricts the opportunity for ETs: $b \to +\infty \Rightarrow P_{0-ET} \to 1$ and $P_{1-\,and\,2-ET} \to 0$ with both ϕ_1 and ϕ_2. Notice that the tails of the P_{0-ET} and P_{1-ET} curves for $b >\approx 7.0$ a.u. with ϕ_1 look similar to their counterparts with ϕ_2. In both symmetry-preserving and symmetry–breaking cases, P_{2-ET} is much lower than P_{0-ET} and P_{1-ET} for all b's and seems to be less affected by symmetry breaking. The symmetry-breaking effects on Mulliken populations and ET probabilities observed in $H^+ + H_2O$ at E_{Lab} = 28.5– 200 eV are similar in trend and form to their counterparts in $H^+ + C_2H_4$ at E_{Lab} = 30 eV[6].

To understand why symmetry breaking favors 1-ET reactions, we should first notice that all symmetry-preserving simulations lead to final projectile Mulliken populations $N_\alpha = N_\beta$, whereas symmetry-breaking simulations lead to $N_\alpha \neq N_\beta$ (cf. Fig. 7). One can analytically corroborate these populations outcomes from our derivation of N_α, N_β and P_{n-ET} in terms of the α and β Thouless parameters $\left\{z_{ph}^{\alpha}(t),\, z_{ph}^{\beta}(t)\right\}$ in Eqs. 17-41 of Ref.[26]; therein, by setting different values of those parameters, one can generate symmetry-conforming and symmetry-broken Thouless states and their corresponding N_α and N_β. A simple mathematical analysis of $P_{1-ET} = N_\alpha\left(1-N_\beta\right)+N_\beta\left(1-N_\alpha\right)$, Eq. (12), proves that its maximum possible value is 0.5 for

$N_\alpha = N_\beta = 0.5$ under the symmetry-imposed constraint $N_\alpha = N_\beta$, but it is 1.0 (absolute maximum) for $N_{\alpha/\beta} = 1$ without such a constraint. Therefore, the 1-ET probability P_{1-ET} can acquire higher values if the symmetry constraints of the Thouless state are broken during evolution.

Having discussed the symmetry-breaking effects on Mulliken populations and ET probabilities, we can discuss those effects on the resulting *n*-ET ICSs. In the case of $H^+ + H_2O$, most of the available experimental *n*-ET ICSs for E_{Lab} = 28.5 - 200.0 eV are 1-ET ICSs; thus, we will concentrate on this type of ICSs. Fig. 9 plots 1-ET ICSs, σ_{1-ET}, from various experimental groups at E_{Lab} = 50[14], 70[14], 100[14, 15], and 200[14-16] eV in comparison with their theoretical counterparts at E_{Lab} = 28.5-200.0 eV from SLEND/6-31G** simulations with ϕ_1 and ϕ_2, and from alternative molecular-orbital close-coupling (MOCC) calculations[31]. The MOCC method solves the time-independent close-coupling scattering equations of $H^+ + H_2O$ employing PESs calculated with the single- and double-excitation configuration interaction (CISD) method[31]. We include these high-level MOCC results[31] to have independent theoretical data for comparison. For a closer inspection, Table 2 lists the SLEND and experimental data in Fig. 9 and the absolute and relative percentage errors of the experiments (when available) at E_{Lab} = 28.5, 48.6, 50[14], 70[14], 100[14, 15] and 200[14-16] eV; in addition, Table 3 lists the relative percentage deviations of all the theoretical results with respect to the experimental ones. Notice that we include among these data the 1-ET ICSs at E_{Lab} = 28.5 and 48.6 eV to assess their corresponding 1-ET DCSs[17] in the Sect. 4.4 below. On inspecting the data in Fig. 9 and Tables 2-3, we find that all the theoretical results are, to some extent, close in value, and that all of them lay below their experimental counterparts. Despite their quite different formalisms, SLEND and MOCC predict 1-ET ICSs in moderate agreement among themselves, a fact that indicates the reliability of these theoretical results. Quantitatively, the agreement of the theoretical methods with the experiments increases in the order: SLEND/6-31G** with ϕ_1 < MOCC < SLEND/6-31G** with ϕ_2, where these methods exhibit average percentage deviations of -

86.76, -69.36 and -64.31 %, respectively (cf. Table 3). While these deviations are considerable, the reader should bear in mind that the experimental data come from miscellaneous scattering setups built with 1960-1970's technology[14-16] that reported relatively dissimilar results (e.g., the experimental σ_{1-ET} at E_{Lab} = 200 eV ranges from 18.0 to 57.0[15] Å^2, cf. Table 2). Perhaps, new measurements with contemporaneous technologies may help to resolve the current divergence between experimental and theoretical data. Reflecting the effects observed in Mulliken populations and ET probabilities, the spin-breaking SLEND/6-31G** simulations with ϕ_2 predict higher values of 1-ET ICSs than their spin-preserving counterparts with ϕ_1. Specifically, the symmetry-breaking augmentation ratio of the 1-ET ICSs: $ratio_{1-ET\ ICS}$ = symmetry-breaking ICS / symmetry-preserving ICS, takes the values: 6.638, 5.187, 4.903, 3.889, 3.422 and 2.124 at E_{Lab} = 28.5, 48.6, 50, 70, 100 and 200 eV, respectively. More significantly, the spin-breaking 1-ET ICSs are closer to the experimental ones than their spin-preserving counterparts. Qualitatively, only the 1-ET ICSs from SLEND/6-31G** with ϕ_2 correctly reproduce the monotonic decreasing pattern of the experimental 1-ET ICSs vs. collision energy; in contrast, SLEND/6-31G** with ϕ_1 and MOCC incorrectly predict a monotonic increasing pattern. The best quantitative and qualitative performance of SLEND/6-31G** with ϕ_2 for 1-ET ICSs predictions endorses the use of the spin-breaking procedure to improve time-dependent ET simulations within the single-determinantal representation. The performance of SLEND/6-31G** with ϕ_2 for 1-ET ICSs is somewhat better than that of MOCC despite the latter's use of high-level CISD PESs; this is likely so because of the approximations adopted in the MOCC dynamics, viz., (1) assuming that H^+ travels in a straight trajectory (SLEND allows all types of trajectories, cf. Figs. 3-6), (2) excluding reactive processes (SLEND allows those processes, cf. Figs. 4-5), and (3) considering only 4 projectile-target orientations (SLEND considers 34 orientations). In general, SLEND performed somewhat better than or comparably to time-independent close-coupling scattering

methods with high-level PESs and similar approximations in their dynamics (e.g., for $H^+ + H_2$[32], N_2[33], CO[34] and NO[35]).

4.3 Scattering Patterns and Rainbow Scattering Angles.

The classical scattering angle function $\theta_{Lab}(b)$ of the outgoing projectile $H_p^{q_1}$ vs. the impact parameter b is of particular interest because it provides details of the scattering dynamics, permits evaluating projectile-target interactions, and helps to interpret the rainbow angle scattering signatures in the DCSs[27] (cf. Sect. 4.4 below). From the initial conditions described in Sect. 3.2, the laboratory-frame scattering angle $\theta_{Lab}(b)$ of the projectile with respect to its initial axis of incidence is

$$\theta_{Lab} = \arccos\left(\frac{\mathbf{P}^i_{H^+} \mathsf{g} \mathbf{P}^f_{H_p^{q_1}}}{\left|\mathbf{P}^i_{H^+}\right|\left|\mathbf{P}^f_{H_p^{q_1}}\right|}\right) \quad (0 \le \theta_{Lab} \le 180°); \qquad (13)$$

where $\mathbf{P}^i_{H^+}$ and $\mathbf{P}^f_{H_p^{q_1}}$ are the momenta of the projectile at initial and final times, respectively. Fig. 10 plots $\theta_{Lab}(b)$ vs. b of selected SLEND/6-31G** simulations of $H^+ + H_2O$ at energy $E_{Lab} = 28.5$ eV from projectile-target orientations (180°,90°,90°) (panel A) and (0°,90°,270°) (panel B), and at energy $E_{Lab} = 48.6$ eV from projectile-target orientations (180°,90°,90°) (panel C) and (0°,90°,270°) (panel D), and with symmetry-breaking parameters ϕ_1 (red curves) and ϕ_2 (blue curves). Fig. 10 exhibits the typical scattering features observed in H^+-molecule collisions[32-39]. Specifically, in all the curves, the sharp minimum at low impact parameters is the secondary rainbow scattering angle θ_{Lab}^{SR} that corresponds to the maximum deflection of the projectile from the initial plane of travelling determined by $\mathbf{R}^{(i)}_{H^+}$ and $\mathbf{P}^{(i)}_{H^+}$ (cf. Fig. 1)[36]; if the projectile remains on such a plane during collision[36], $\theta_{Lab}^{SR} = 0^0$ and is the glory scattering angle[27]. In addition, in all the curves, the tall rounded maximum to the right of the θ_{Lab}^{SR} position is the primary rainbow scattering angle θ_{Lab}^{PR} that corresponds to the maximum projectile-target attractive

scattering[27]. Fig. 10 reveals that symmetry breaking has a mild effect on $\theta_{Lab}(b)$. Specifically, all the $\theta_{Lab}(b)$ curves moderately shrink down in the right part of the plots as symmetry breaking takes place; as a result, all the primary rainbow scattering angles θ_{Lab}^{PR} slightly decrease in value by symmetry breaking. On the other hand, all the $\theta_{Lab}(b)$ curves practically do not change in the left part of the plots as symmetry breaking takes place; as a result, all the secondary rainbow scattering angles θ_{Lab}^{SR} remain virtually unchanged by symmetry breaking. The changes of the $\theta_{Lab}(b)$ functions of $H^+ + H_2O$ at E_{Lab} = 28.5–200 eV by symmetry breaking are similar in trend and form to the changes in their counterparts in $H^+ + C_2H_4$ at E_{Lab} = 30 eV by the same procedure[6]. However, the changes were of a higher magnitude in $H^+ + C_2H_4$, to the point that secondary rainbow scattering angles did perceptibly decrease in that system. In any case, in both systems, the observed changes in $\theta_{Lab}(b)$ result from the different projectile-target interaction forces with and without symmetry breaking (for more details on this subject, cf. Sect. 4.3 of Ref. [6]).

4.4. Non-electron-transfer and electron-transfer differential cross sections

One of the most important experimental data of $H^+ + H_2O$ at E_{Lab} = 28.5 and 48.6 eV is the total 0- and 1-ET DCSs[17]. In SLEND, the n-ET DCS $d\sigma_{(\alpha,\beta,\gamma)}^{n-ET}(\theta_{CM})/d\Omega$ of the set of simulations from the projectile-target orientation (α,β,γ) is calculated in the center-of-mass (CM) frame as[27]:

$$\frac{d\sigma_{(\alpha,\beta,\gamma)}^{n-ET}(\theta_{CM})}{d\Omega} = \frac{1}{4k_i^2}\left|\sum_{l=0}^{\infty}(2l+1)\ T_{(\alpha,\beta,\gamma)}^{n-ET}(l)\,P_l(\cos\theta_{CM})\right|^2 \qquad (14)$$

where k_i is the projectile initial wave vector magnitude, l is an orbital angular momentum quantum number, $T_{(\alpha,\beta,\gamma)}^{n-ET}(l)$ is the T-matrix, and $P_l(\cos\theta_{CM})$ are Legendre polynomials. Since SLEND adopts a

classical nuclear dynamics, the l values are obtained from the impact parameters b via the semi-classical expression $l = k_i b$ [27]. In SLEND, $T^{n-ET}_{(\alpha,\beta,\gamma)}(l)$ is

$$T^{n-ET}_{(\alpha,\beta,\gamma)}(l = k_i b) = \sqrt{P_{n-\mathrm{ET}}(\alpha,\ \beta,\ \gamma, b)}\exp\left[i2\eta_{(\alpha,\beta,\gamma)}(l = k_i b)\right] \quad (15)$$

where $P_{n-\mathrm{ET}}(\alpha,\ \beta,\ \gamma, b)$ are the n-ET probabilities from Eq. (12), and $\eta_{(\alpha,\beta,\gamma)}(l)$ is the phase shift obtained from the semi-classical expression $\Theta_{CM}(b) = (2/k_i)\left[\partial\eta(b)/\partial b\right]$, where $\left|\Theta_{CM}(b)\right| = \theta_{CM}(b)$ is the classical deflection function[27]. The CM DCSs $d\sigma^{n-ET}_{(\alpha,\beta,\gamma)}(\theta_{CM})/d\Omega$ are calculated with Eqs. (14)-(15) using the SLEND simulation data transformed into the CM frame. The resulting $d\sigma^{n-ET}_{(\alpha,\beta,\gamma)}(\theta_{CM})/d\Omega$ are transformed back into the laboratory frame and averaged over all orientations to obtain the n-ET DCSs $d\bar{\sigma}^{n-ET}_{SLEND}(\theta_{Lab})/d\Omega$ in that frame.

Fig. 11 plots the total 0- and 1-ET DCSs, $d\bar{\sigma}^{n-ET}_{SLEND}(\theta_{Lab})/d\Omega$, of $H^+ + H_2O$ at E_{Lab} = 28.5 eV (panels A and B) and 48.6 eV (panels C and D) from the only available experiment[17] and from SLEND/6-31G** simulations with symmetry-breaking parameters ϕ_1 (panels A and C) and ϕ_2 (panels B and D) vs. the scattering angle θ_{Lab}. Fig. 11 also indicates the positions and values of the primary rainbow scattering peaks and angles, respectively. The experimental DCSs were reported in relative units[17]. Therefore, to allow comparison, we follow the standard practice of normalizing the experimental 0- and 1-ET DCSs with respect to their corresponding theoretical counterparts in each panel. These normalizations seek to obtain minimum standard deviations between experimental and theoretical DCSs over all the scattering angles investigated in the experiment: $0^0 \leq \theta_{Lab} \leq 8^0$ [17]; the minimum standard deviations achieved in the normalizations are reported in the captions of Fig. 11. Inspection of these figures reveals that symmetry breaking has a considerable effect on the SLEND/6-31G** 0- and 1-ET DCS values: the former decrease and the latter increase as symmetry breaking occurs. Specifically, for E_{Lab} = 28.5 eV, the

SLEND/6-31G** 0- and 1-ET DCSs with ϕ_1 appear well separated and display the order 0-ET DCS > 1-ET DCS for all θ_{Lab} ; on the other hand, the same DCSs with ϕ_2 appear much closer and display the reversed order 1-ET DCS > 0-ET DCS with a small separation (and a few order exceptions) for $2^0 \leq \theta_{Lab} \leq 6^0$, and with a larger separation for $\theta_{Lab} > 6^0$. For E_{Lab} = 48.6 eV, the SLEND/6-31G** 0- and 1-ET DCSs show the same behavior with symmetry breaking and a reversed order 1-ET DCS > 0-ET DCS with ϕ_2 for $\theta_{Lab} > 2^0$. We observed the same order inversion in the SLEND 0- and 1-ET DCSs with symmetry breaking for $\theta_{Lab} > 2^0$ in $H^+ + C_2H_4$ at E_{Lab} = 30 eV[6]. The increase of the SLEND/6-31G** 1-ET DCSs by symmetry breaking is consistent with the increase in the ET processes by the same procedure observed in Mulliken populations, ET probabilities, and 1-ET ICSs (cf. Sect. 4.2). The reciprocal changes of the SLEND/6-31G** 0- and 1-ET DCSs by symmetry breaking (the former decreases as the latter increases) is easy to understand from the role played by the $_n$-ET probabilities $P_{n-\mathrm{ET}}(\alpha, \beta, \gamma, b)$, $0 \leq n \leq 2$, in the DCSs Eqs. (14)-(15). Specifically, since $P_{2-\mathrm{ET}}$ is negligible (cf. Fig. 8), if $P_{1-\mathrm{ET}}$ increases then $P_{0-\mathrm{ET}}$ must decreases to keep the total probability as $\sum_{n=0}^{2} P_{n-\mathrm{ET}} = 1$ [cf. Eq. (12) and Fig. 8] so that their corresponding 0- and 1-ET DCSs change analogously [cf. Eqs. (14)-(15)]. For E_{Lab} = 28.5 eV, the experimental 0- and 1-ET DCSs show no primary rainbow scattering peaks within the range of the investigated scattering angles: $0^0 \leq \theta_{Lab} \leq 8^0$ [17]. Despite that, the experimentalists speculated from their measured data that a primary rainbow scattering peak should exist slightly outside that range at $\theta_{Lab}^{PR} \approx 8.5^0$ [17]. For E_{Lab} = 28.5 eV, the SLEND/6-31G** 0- and 1-ET DCSs with ϕ_1 show primary rainbow scattering peaks at $\theta_{Lab}^{PR} = 9.5^0$, and the SLEND/6-31G** 0- and 1-ET DCSs with ϕ_2 show those peaks at $\theta_{Lab}^{PR} = 9.0^0$. These theoretical values agree well with their experimental counterpart $\theta_{Lab}^{PR} \approx 8.5^0$ given the speculative nature of the latter. It is remarkable that the present SLEND simulations can validate this primary rainbow

scattering angle estimation from the experimental data[17]. Similar to the $H^+ + C_2H_4$ case[6], the theoretical θ_{Lab}^{PR} from DCSs with symmetry breaking agree better with the experimental θ_{Lab}^{PR} . For $E_{Lab} = 48.6$ eV, the experimental 0- and 1-ET DCSs show primary rainbow scattering peaks at $\theta_{Lab}^{PR} = 5.0^0$ [17]. For the same energy, the SLEND/6-31G** 0- and 1-ET DCSs with ϕ_1 show primary rainbow scattering peaks at $\theta_{Lab}^{PR} = 5.3^0$, and the SLEND/6-31G** 0- and 1-ET DCSs with ϕ_2 show those peaks at $\theta_{Lab}^{PR} = 5.7^0$. These theoretical values agree well with their experimental counterpart $\theta_{Lab}^{PR} = 5^0$. In this case, the theoretical θ_{Lab}^{PR} with symmetry preservation agrees slightly better with the experimental θ_{Lab}^{PR} ; however, this fact may not be significant given the proximity of the two theoretical values. As already observed in the scattering functions $\theta_{Lab}(b)$, symmetry breaking mildly affect the values of the theoretical primary rainbow scattering angles in the present system.

With the exception of the θ_{Lab}^{PR} at $E_{Lab} = 48.6$ eV, the symmetry breaking effects on the SLEND/6-31G** 0- and 1-ET DCSs of $H^+ + H_2O$ at $E_{Lab} = 28.5$ and 48.6 eV are identical in trend and form to those on the corresponding DCSs of $H^+ + C_2H_4$ at $E_{Lab} = 30$ eV[6]. In both scattering systems, the fact that only relative (non-absolute) experimental DCSs are available complicates the assessment of what type of SLEND DCSs is more accurate: those from symmetry-preserving simulations or from symmetry-breaking ones. In the case of $H^+ + C_2H_4$, the analysis of the standard deviations between SLEND and experimental DCSs, and the comparison of the SLEND and experimental primary rainbow scattering angles clearly showed that the SLEND/6-31G** 0- and 1-ET DCSs from symmetry-breaking simulations agree much better with the experimental data[6]. In fact, the lower accuracy of the SLEND/6-31G** 0- and 1-ET DCSs from symmetry-preserving simulations was perceptible by direct inspection of their plots[6]. In $H^+ + H_2O$, the standard deviations between SLEND and experimental 0-ET DCSs considerably decrease with symmetry-breaking at the two considered energies (cf. captions of Fig. 11); thus, the SLEND 0-ET DCSs' accuracy improves

under symmetry breaking. On the other hand, the corresponding standard deviations in the 1-ET DCSs increase with symmetry breaking at the two considered energies. While this may suggest an accuracy diminution with symmetry breaking, we should first notice that the standard deviation may be a less reliable metric for accuracy in the 1-ET case due to the high oscillations in some of the experimental and SLEND 1-ET DCSs; moreover, the accuracy of the experimental 1-ET DCSs may be lower due to their measurement with a detector in principle designed for final H^+ projectiles (0-ETs) and not for H ones (1-ETs)[17, 36]. In Sect. 4.2, we observed that the SLEND/6-31G** 1-ET ICSs of $H^+ + H_2O$ with symmetry breaking agree better with the experimental 1-ET ICSs at various energies. This is a significant result because, unlike the experimental DCSs, the experimental ICSs are in absolute units. Since an ICS is essentially the integral of its corresponding DCS over θ_{Lab} [27], we can assume that all the current SLEND 1-ET DCSs with symmetry breaking should be more accurate than those with symmetry preservation. Then, from all the above observations, we conclude that the SLEND/6-31G** 0- and 1-ET DCSs of $H^+ + H_2O$ at E_{Lab} = 28.5 and 48.6 eV with symmetry breaking are the more accurate SLEND DCSs from the present simulations.

5. Conclusions, Further Remarks, and Future Research

We presented a SLEND investigation of $H^+ + H_2O$ at E_{Lab} = 28.5 – 200.0 eV in conjunction with a computational procedure that induces symmetry breaking during the dynamics evolution[6]. The studied system is a computationally feasible prototype to simulate water radiolysis reactions in ICT[18-20]. The symmetry-breaking procedure introduces a low degree of symmetry breaking into the electronic RHF state of the reactants to induce a higher degree of symmetry breaking during the subsequent dynamics. This initial symmetry-broken state corresponds to the ASDW state in Fukutome's classification of symmetry breakings in single-determinantal states[1]. In all cases, simulations starting from symmetry-conforming states preserved that symmetry during evolution, whereas simulations starting from symmetry-broken states exhibited an upsurge of symmetry breaking by the time of the reactants' collision. Notably,

symmetry breaking considerably favored target-to-projectile 1-ET processes over the 0-ET ones as revealed by Mulliken populations and ET probabilities. As a result, 1-ET ICSs and 1-ET DCSs increased in value under symmetry breaking, whereas 0-ET DCSs and rainbow scattering angles decreased. Overall, all these properties agreed better with experimental results[14-17] if predicted from symmetry-breaking simulations. Remarkably, SLEND 1-ET ICSs from symmetry-breaking simulations agreed somewhat better with experimental data[14-16] than 1-ET ICSs calculated with the high-level MOCC method[31]. These more accurate results endorse the use of our spin-breaking procedure to improve time-dependent simulations of ET reactions within the single-determinantal representation.

In our SLEND studies on $H^+ + H_2O$ (current one) and $H^+ + C_2H_4$ (Ref.[6]), we demonstrated that symmetry breakings occurring during the time evolution of a single-determinantal state influence the fate of the simulated reactions and improve the accuracy of their dynamical properties. In those efforts, we devised a rigorous procedure to induce the aforesaid symmetry breakings in a controlled form by varying the parameters of an initial Thouless single-determinantal state[5]; those parameters quantify the initial degree of symmetry breaking. In the time-independent realm, Fukutome[1] revealed all the possible symmetry breakings in a single-determinantal state that allow or facilitate phenomena otherwise hindered by symmetry constraints. In his investigation[1], Fukutome took advantage of the Thouless representation[5] to generate all sorts of symmetry breakings in his targeted states. We have extended Fukutome analysis of symmetry breakings to the time-dependent realm by time-evolving the Thouless single-determinantal state within the SLEND framework. Ultimately, our symmetry-breaking procedure provides an efficient tool to generate and investigate time-dependent symmetry breakings in chemical reactions, and to improve the prediction of dynamical properties through those breakings. This tool is not exclusive of the SLEND method because, through the Thouless representation[5], it can be adapted to any time-dependent, non-adiabatic method that evolves a single-determinantal state. We will further develop the theory of time-

dependent symmetry breakings and systematically apply our procedure to various types of chemical reactions in a sequel to this publication.

CONFLICTS OF INTEREST

There are no conflicts of interest to declare.

ACKNOWLEDGEMENTS

All present calculations have been performed at the Texas Tech University High Performance Computer Center. JCD acknowledges partial financial support from the National Science Foundation Graduate Research Fellowship Program (DGE 2140745). EDS thanks financial support from the CAPES program of the Federal Government of Brazil. JAM acknowledges partial financial support for this research from the National Institutes of Health (NIH) grant 1R15GM128149-01.

References

1. H. Fukutome, *Int. J. Quantum Chem.*, 1981, **20**, 955-1065.
2. R. McWeeny, *Methods of Molecular Quantum Mechanics*, Academic Press, London, 2nd edn., 1992.
3. A. Szabo and N. S. Ostlund, *Modern Quantum Chemistry: Introduction to Advanced Electronic Structure Theory*, Dover Publications Inc, Mineola, NY, 1st, rev edn., 1989.
4. B. Weiner and S. B. Trickey, *Int. J. Quantum Chem.*, 1998, **69**, 451-460.
5. D. J. Thouless, *Nucl. Phys.*, 1960, **21**, 225-232.
6. P. M. McLaurin, R. Merritt, J. C. Dominguez, E. S. Teixeira and J. A. Morales, *Physical Chemistry Chemical Physics*, 2019, **21**, 5006.
7. E. Deumens, A. Diz, R. L. Longo and Y. Öhrn, *Rev. Mod. Phys.*, 1994, **66**, 917-983.
8. C. Stopera, T. V. Grimes, P. M. McLaurin, A. Privett and J. A. Morales, *Adv. Quantum Chem.*, 2013, **Vol. 66, Chapter 3**, 113-149.
9. F. Hagelberg, *Electron Dynamics in Molecular Interactions: Principles and Applications* World Scientific, Singapure, 1 edn., 2014.
10. P. Kramer and M. Saraceno, *Geometry of The Time-Dependent Variational Principle in Quantum Mechanics*, Springer-Verlag, New York, 1981.
11. P. M. McLaurin, *PhD Dissertation, Texas Tech University, Department of Chemistry and Biochemistry*, 2011.
12. A. Privett, *PhD Dissertation, Texas Tech University, Department of Chemistry and Biochemistry, Lubbock, Texas*, 2015.
13. R. Merritt, *MS Thesis, Texas Tech University, Department of Chemistry and Biochemistry, Lubbock, Texas*, 2017.
14. C. F. Barnett, J. A. Ray, E. Ricci, M. I. Wilker, E. W. McDaniel, E. W. Thomas and H. B. Gilbody, *Atomic Data for Controlled Fusion Research*, Oak Ridge National Laboratory, 1977.
15. M. A. Coplan and K. W. Ogilvie, *J. Chem. Phys.*, 1970, **52**, 4154-4160.
16. P. G. Cable, *Ph.D. Thesis, University of Maryland*, 1967.

17. B. Friedrich, G. Niedner, M. Noll and J. P. Toennies, *J. Chem. Phys.*, 1987, **87**, 5256-5265.
18. W. P. Levin, H. Kooy, J. S. Loeffler and T. F. DeLaney, *British Journal of Cancer* 2005, **93**, 849-854.
19. S. Girdhani, R. Sachs and L. Hltaky, *Radiation Research* 2013, **179**, 257-272.
20. O. Jäkel, *Radiat. Prot. Dosim.*, 2009, **137**, 156-166.
21. A. Privett and J. A. Morales, *Chemical Physics Letters* 2014, **603**, 82-88.
22. P. M. McLaurin, A. Privett, C. Stopera, T. V. Grimes, A. Perera and J. A. Morales, *Mol. Phys.*, 2015, **113**, 297-313.
23. A. Privett, E. S. Teixeira, C. Stopera and J. A. Morales, *PLoS One*, 2017, **12**, e0174456.
24. E. Teixeira, K. Uppulury, A. Privett, C. Stopera, P. M. McLaurin and J. A. Morales, *Cancers*, 2018, **10**, 136.
25. E. S. Teixeira and J. A. Morales, *Theor. Chem. Acc.*, 2020, **139**, 73.
26. E. D. Silva, P. M. McLaurin and J. A. Morales, *J. Chem. Phys.*, 2021, **155**, 124112.
27. M. S. Child, *Molecular Collision Theory*, Academic Press, Inc., New York, 1 edn., 1974.
28. R. Longo, A. Diz, E. Deumens and Y. Öhrn, *Chem. Phys. Lett.*, 1994, **220**, 305-311.
29. R. N. Zare, *Angular Momentum, Understanding Spatial Aspects in Chemisty and Physics*, Wilesy-Interscience Publication, New York, 1988.
30. S. Mamone, G. Pileio and M. H. Levitt, *Symmetry*, 2010, **2**, 1423-1449.
31. S. Mada, K.-N. Hida, M. Kimura, L. Pichl, H.-P. Liebermann, Y. Li and R. J. Buenker, *Phys. Rev. A*, 2007, **75**, 022706.
32. J. A. Morales, A. Diz, E. Deumens and Y. Öhrn, *J. Chem. Phys.*, 1995, **103**, 9968-9980.
33. C. Stopera, B. Maiti, T. V. Grimes, P. M. McLaurin and J. A. Morales, *J. Chem. Phys.*, 2011, **134**, 224308.
34. C. Stopera, B. Maiti, T. V. Grimes, P. M. McLaurin and J. A. Morales, *J. Chem. Phys.*, 2012, **136**, 054304.
35. C. Stopera, B. Maiti and J. A. Morales, *Chem. Phys. Lett.*, 2012, **551**, 42-49.
36. G. Niedner, M. Noll, J. P. Toennies and C. Schlier, *J. Chem. Phys.*, 1987, **87**, 2685-2694.
37. J. A. Morales, B. Maiti, Y. Yan, K. Tsereteli, J. Laraque, S. Addepalli and C. Myers, *Chem. Phys. Lett.*, 2005, **414**, 405-411.
38. B. Maiti, R. Sadeghi, A. Austin and J. A. Morales, *Chem. Phys.*, 2007, **340**, 105-119.
39. B. Maiti, P. M. McLaurin, R. Sadeghi, S. Ajith Perera and J. A. Morales, *Int. J. Quantum Chem.*, 2009, **109**, 3026-3035.

Table 1: Selected values of the symmetry breaking parameter ϕ of the initial ASDW reference state $\left|\bar{0}\right\rangle_{ASDW}$ of H_2O along with their spin contaminations and degrees of symmetry breaking of that state.

Symmetry Breaking Parameter ϕ (deg.)	**Spin Contamination** $\left\langle \hat{S}^2(\phi)\right\rangle$ (a.u.)	**Degree of Symmetry Breaking**
$\phi_1 = 0^0$	0.00000000	None
$\phi_2 = 10.24157218^0$	0.12245227	Low

Table 2: SLEND/6-31G** one-electron-transfer (1-ET) integral cross sections σ_{1-ET} from symmetry-preserving (ϕ_1) and symmetry-breaking (ϕ_2) simulations along with available experimental values: Experiment 1 by Barnett et al. (1977)[14], Experiment 2 by Coplan et al. (1970)[15], and Experiment 3 by Cable (1967)[16].

Energy (eV)	**SLEND** ϕ_1 σ_{1-ET} (Å^2)	**SLEND** ϕ_2 σ_{1-ET} (Å^2)	**Experiment 1** σ_{1-ET} (absolute, relative error) (Å^2)	**Experiment 2** σ_{1-ET} (absolute, relative error) (Å^2)	**Experiment 3** σ_{1-ET} (absolute, relative error) (Å^2)
28.5	2.76	18.52	NA	NA	NA
48.6	3.15	16.34	NA	NA	NA
50	3.18	15.59	30.0 ($\pm$ 7.5, 25%)	NA	NA
70	3.43	13.34	29.0 ($\pm$ 7.25, 25%)	NA	NA
100	3.74	12.80	28.0 ($\pm$ 7.0, 25%)	76. ($\pm$ 18.0, 23.7%)	NA
200	4.52	9.62	26.0 ($\pm$ 6.5, 25%)	57. ($\pm$ 18.0, 31.6%)	18. (Not Reported)

Table 3: Relative percentage deviations (RPDs) of the theoretical one-electron-transfer (1-ET) integral cross sections σ_{1-ET} from SLEND/6-31G** simulations with symmetry preservation (ϕ_1) and symmetry breaking (ϕ_2) and from molecular-orbit close-coupling (MOCC) calculations by Mada et al. (2007)[31] with respect to available experimental data: Experiment 1 by Barnett et al. (1977)[14], Experiment 2 by Coplan et al. (1970)[15], and Experiment 3 by Cable (1967)[16].

Theory σ_{1-ET}	**RPD from Expt. 1 (50 eV)**	**RPD from Expt. 1 (70 eV)**	**RPD from Expt. 1 (100 eV)**	**RPD from Expt. 1 (200 eV)**	**RPD from Expt. 2 (100 eV)**	**RPD from Expt. 2 (200 eV)**	**RPD from Expt. 3 (200 eV)**	**Average RPD**
SLEND ϕ_1	-89.41	-88.17	-86.63	-82.63	-95.08	-92.08	-74.91	-86.76
SLEND ϕ_2	-48.04	-54.00	-54.27	-62.99	-83.15	-83.12	-46.55	-64.31

MOCC	-75.66	-68.34	-61.70	-55.59	-85.89	-79.74	-35.86	-69.36

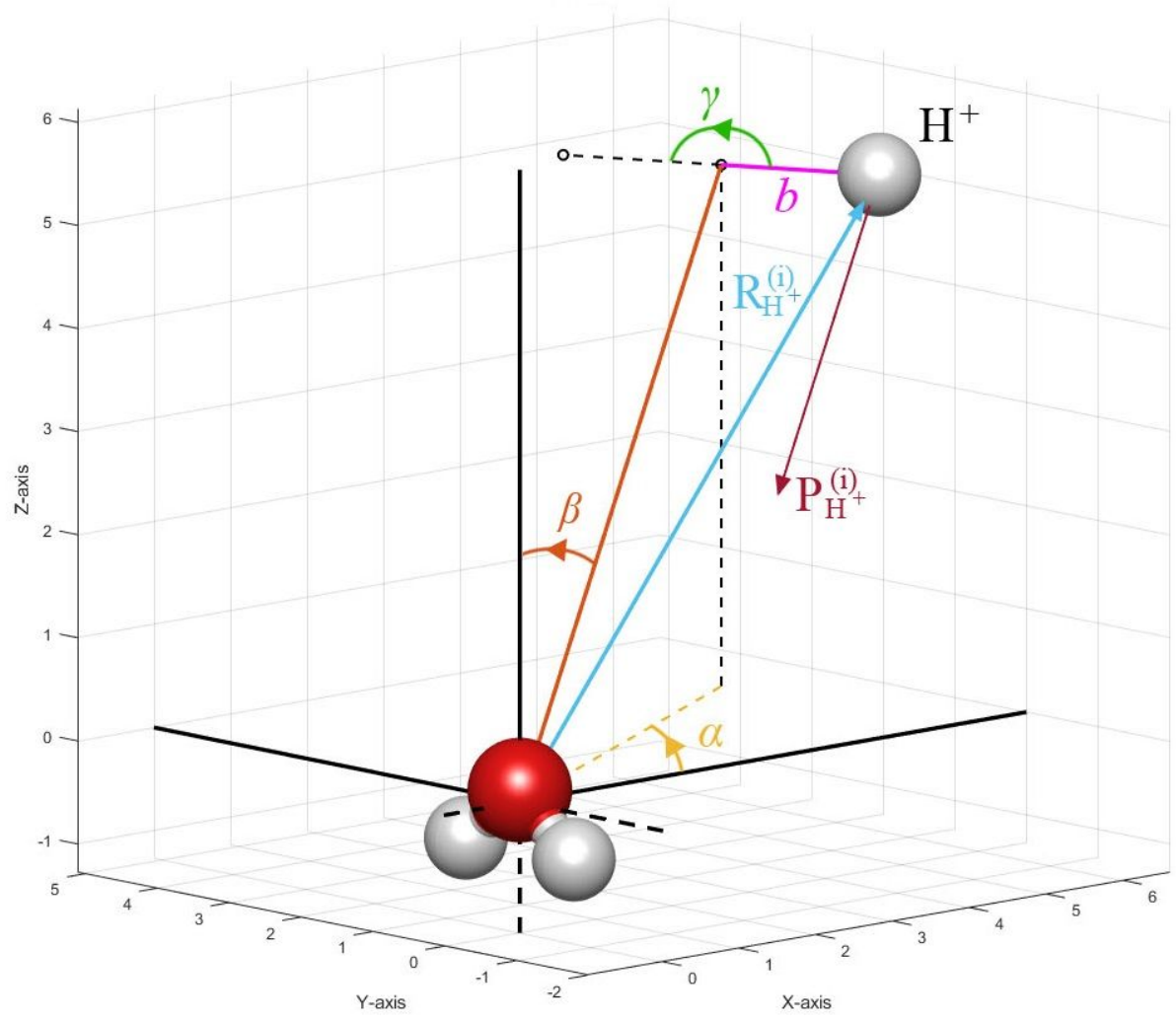

Figure 1: Reactants initial conditions for $H^+ + H_2O$. Colored spheres represent the classical nuclei: O nucleus (red), H nuclei initially in H_2O (white), and H^+ projectile (white). The last particle is prepared with initial position $\mathbf{R}_{H^+}^{(i)}$, initial momentum $\mathbf{P}_{H^+}^{(i)}$, impact parameter b and Euler-angles orientation (α,β,γ) with respect to the H_2O target (cf. text for more details). The projectile initially travels in parallel to an axis of incidence in the direction (α,β) (orange line) and with lateral separation b from that axis.

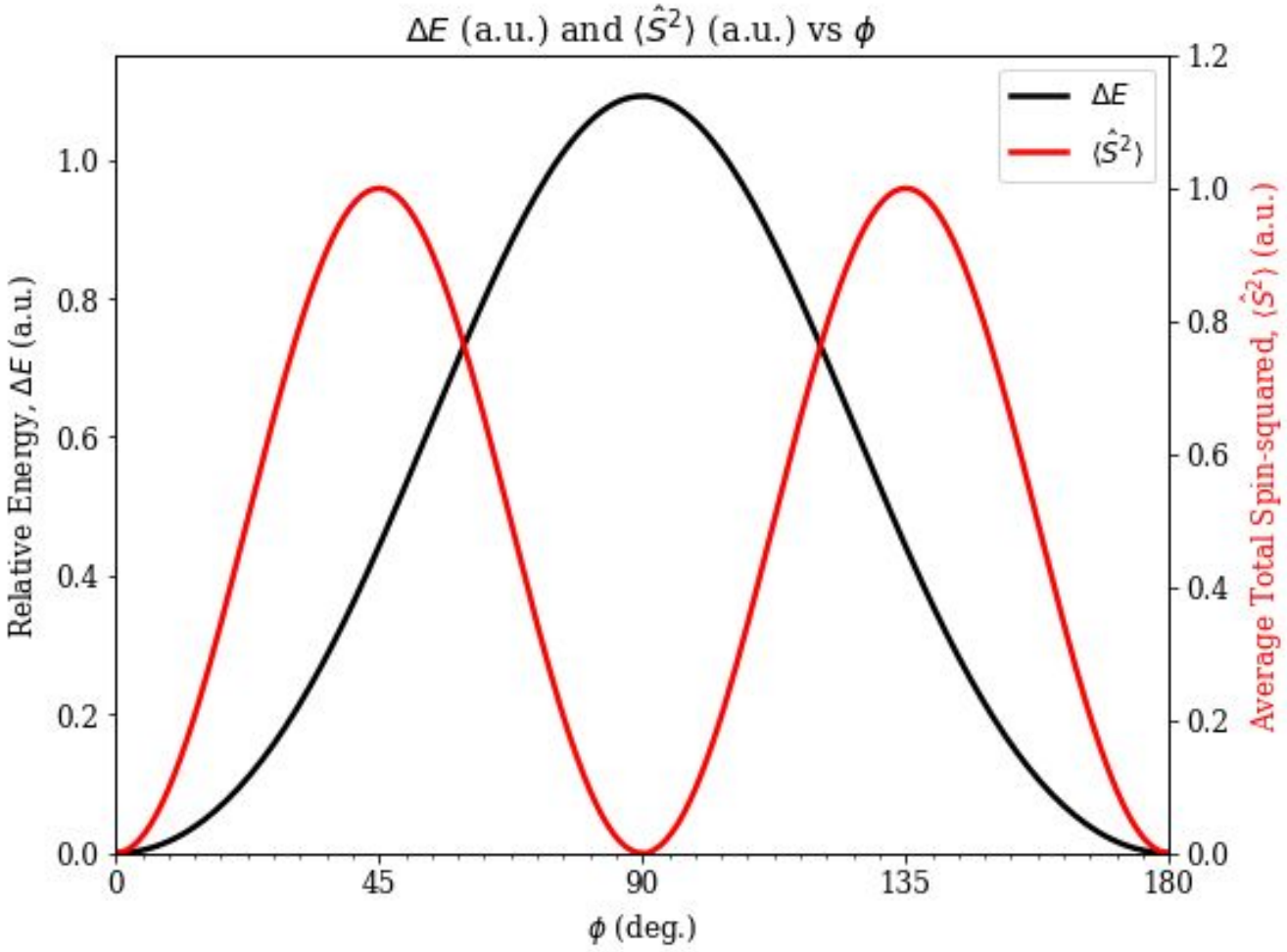

Figure 2: H_2O Hartree-Fock/6-31G** relative energy ΔE with respect to its ground-state value at equilibrium geometry and H_2O average squared total spin $\left\langle \hat{S}^2 \right\rangle$ vs. the symmetry-breaking parameter ϕ.

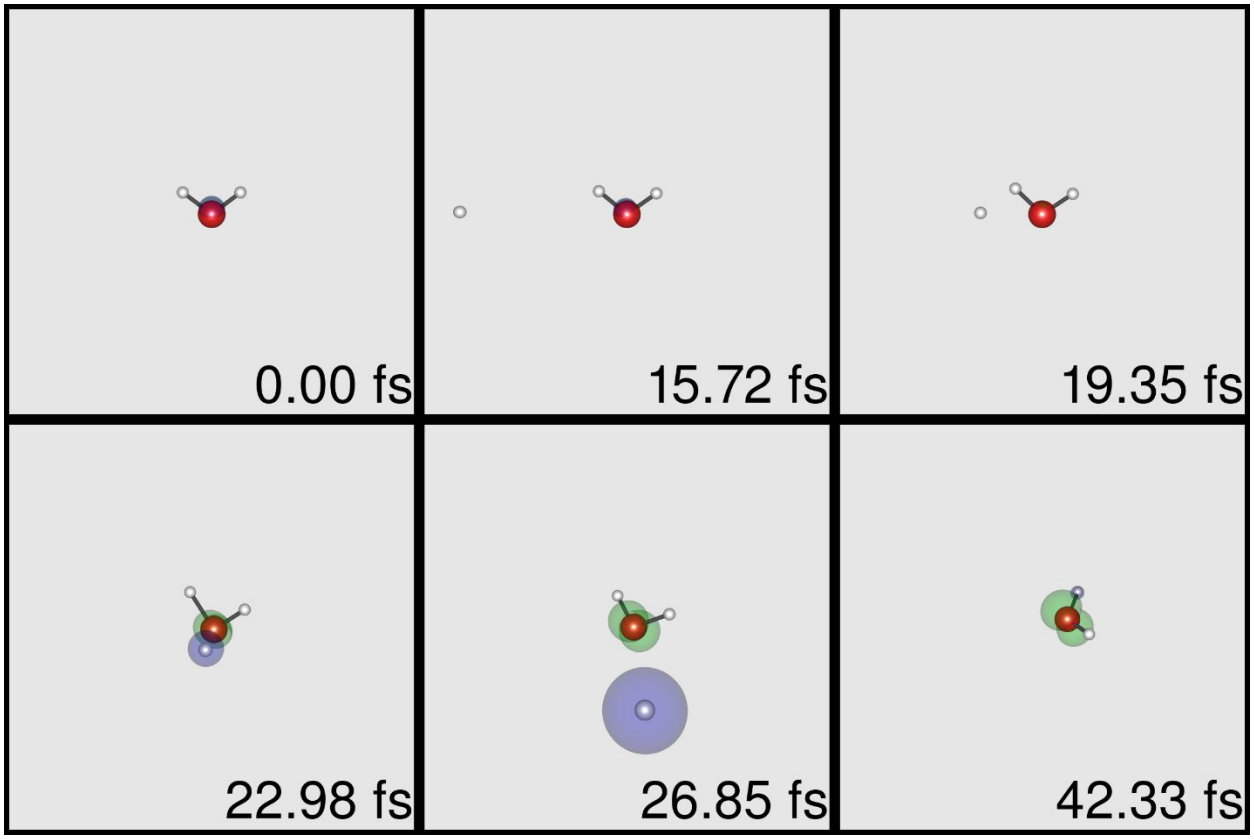

Figure 3: Six sequential snapshots of the SLEND/6-31G** simulation of $H^+ + H_2O$ at $E_{Lab} = 28.5$ eV from projectile-target orientation (180°,270°,0°), projectile impact parameter $b = 0.5$ a.u., and symmetry-breaking parameter $\phi_2 = 10.24...°$ (low initial symmetry breaking).Colored spheres represent the nuclei (red = O, white = H) and colored clouds are isosurfaces of the spin density $|\rho_s| = 0.025$ (green and purple clouds are for ρ_s and $-\rho_s$, respectively). This is an example of a simple projectile scattering, the incoming projectile H^+ collides with H_2O and scatters away without producing a H_2O fragmentation (Reaction I). The time in femtoseconds of each snapshot is shown in the lower right corner of each frame. For the full reaction interpretation, cf. Sect. 4.1.

Figure 4: Six sequential snapshots of the SLEND/6-31G** simulation of $H^+ + H_2O$ at $E_{Lab} = 28.5$ eV from projectile-target orientation (237.6°,306.0°,237.6°), projectile impact parameter $b = 1.9$ a.u., and symmetry-breaking parameter $\phi_2 = 10.24...°$ (low initial symmetry breaking). Colored spheres represent the nuclei (red = O, white = H) and colored clouds are isosurfaces of the spin density $|\rho_s| = 0.025$ (green and purple clouds are for ρ_s and $-\rho_s$, respectively). This is an example of hydrogen substitution, the H^+ projectile substitutes one of the H atoms of H_2O (Reaction II). The time in femtoseconds of each snapshot is shown in the lower right corner of each frame. For the full reaction interpretation, cf. Sect. 4.1.

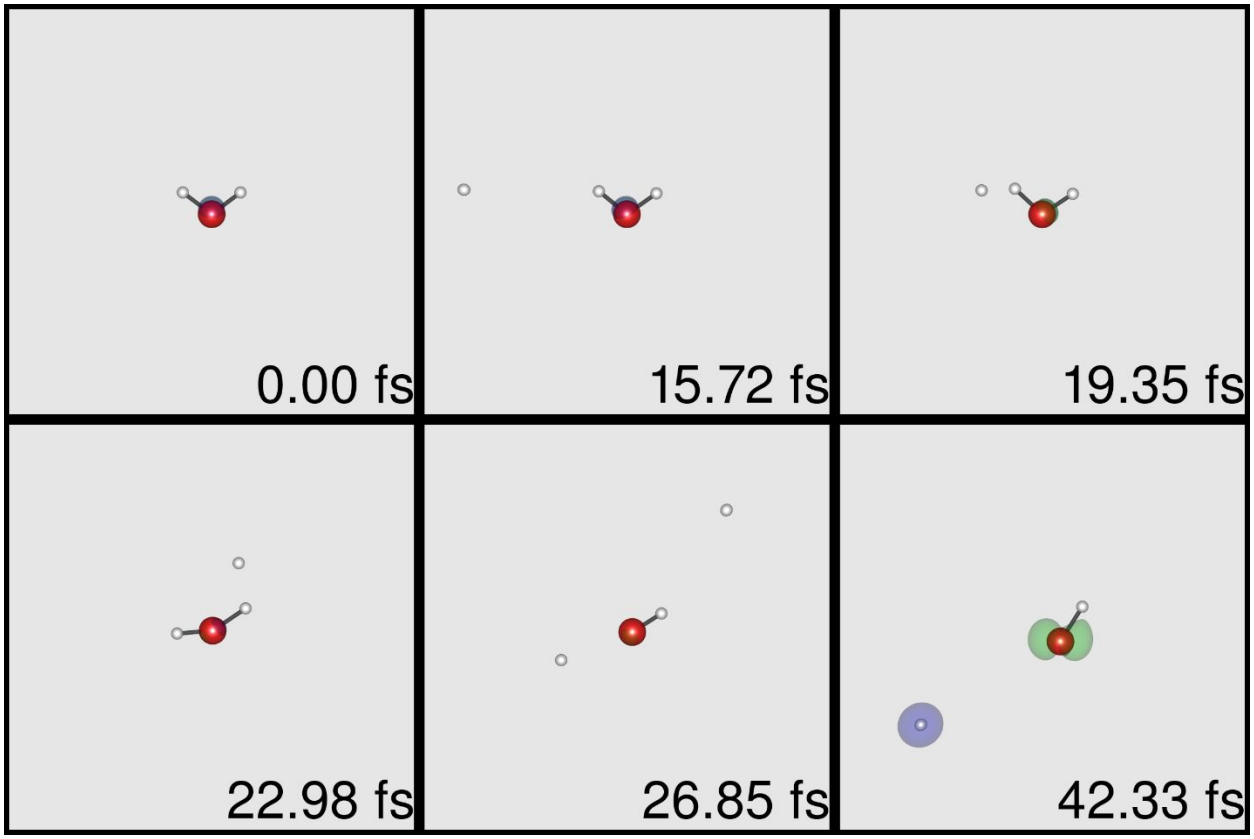

Figure 5: Six sequential snapshots of the SLEND/6-31G** simulation of $H^+ + H_2O$ at $E_{Lab} = 28.5$ eV from projectile-target orientation (0°,90°,270°), projectile impact parameter $b = 1.1$ a.u., and symmetry-breaking parameter $\phi_2 = 10.24...°$ (low initial symmetry breaking). Colored spheres represent the nuclei (red = O, white = H) and colored clouds are isosurfaces of the spin density $|\rho_s| = 0.025$ (green and purple clouds are for ρ_s and $-\rho_s$, respectively). This is an example of a collision-induced water radiolysis reaction into H and OH fragments (Reaction III). The time in femtoseconds of each snapshot is shown in the lower right corner of each frame. For the full reaction interpretation, cf. Sect. 4.1

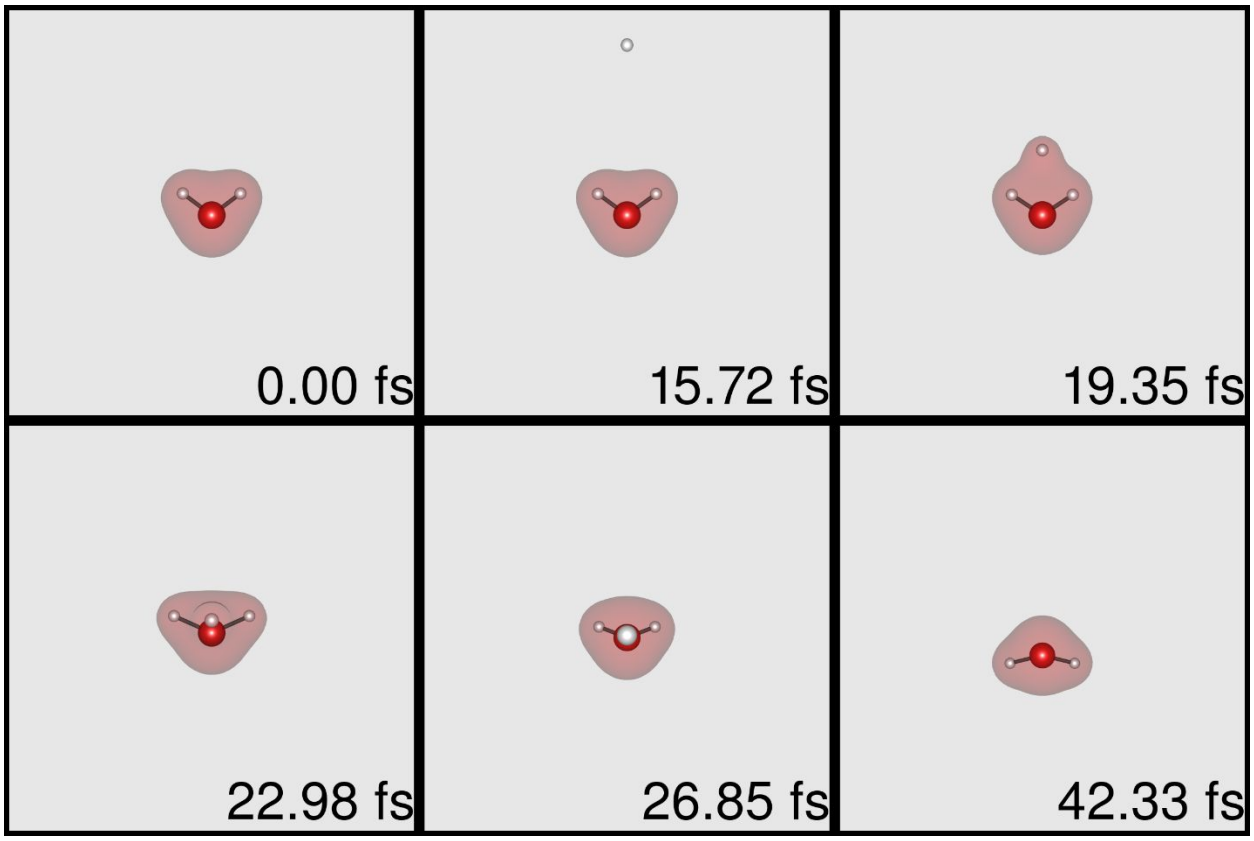

Figure 6: Six sequential snapshots of the SLEND/6-31G** simulation of $H^+ + H_2O$ at $E_{Lab} = 28.5$ eV from the projectile-target orientation (0°,0°,0°), projectile impact parameter $b = 0.5$ a.u., and symmetry-breaking parameter $\phi_1 = 0°$ (no initial symmetry breaking). The colored spheres represent the nuclei (red = O, white = H), and the red cloud is an isosurface of the total electron density $\rho_T = 0.025$. This is an example of a simple projectile scattering, the incoming projectile H^+ collides with H_2O and scatters away without producing a H_2O fragmentation (Reaction I). The time in femtoseconds of each snapshot is shown in the lower right corner of each frame. For the full reaction interpretation, cf. Sect. 4.1.

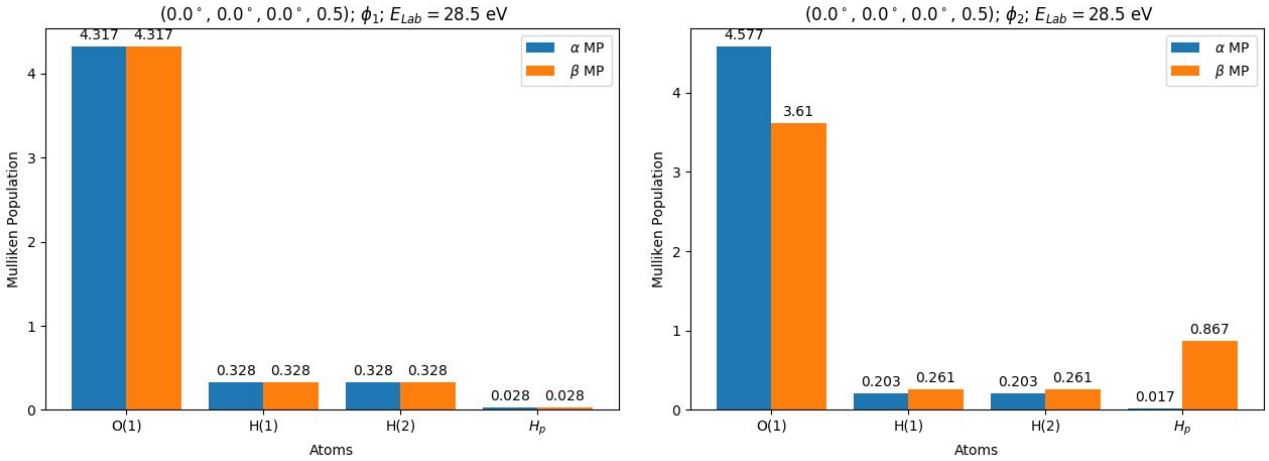

Figure 7: Final α (blue bars) and β (orange bars) electron Mulliken populations on the nuclei of the final target H_2O [labeled O(1), H(1), and H(2)] and on the final outgoing projectile (labeled H_p^+) in SLEND/6-31G** simulations of $H^+ + H_2O$ at $E_{Lab} = 28.5$ eV from orientation (0°,0°,0°), impact parameter $b = 0.5$ a.u., and symmetry-breaking parameters ϕ_1 (symmetry-preserving dynamics, left panel) and ϕ_2 (symmetry-breaking dynamics, right panel).

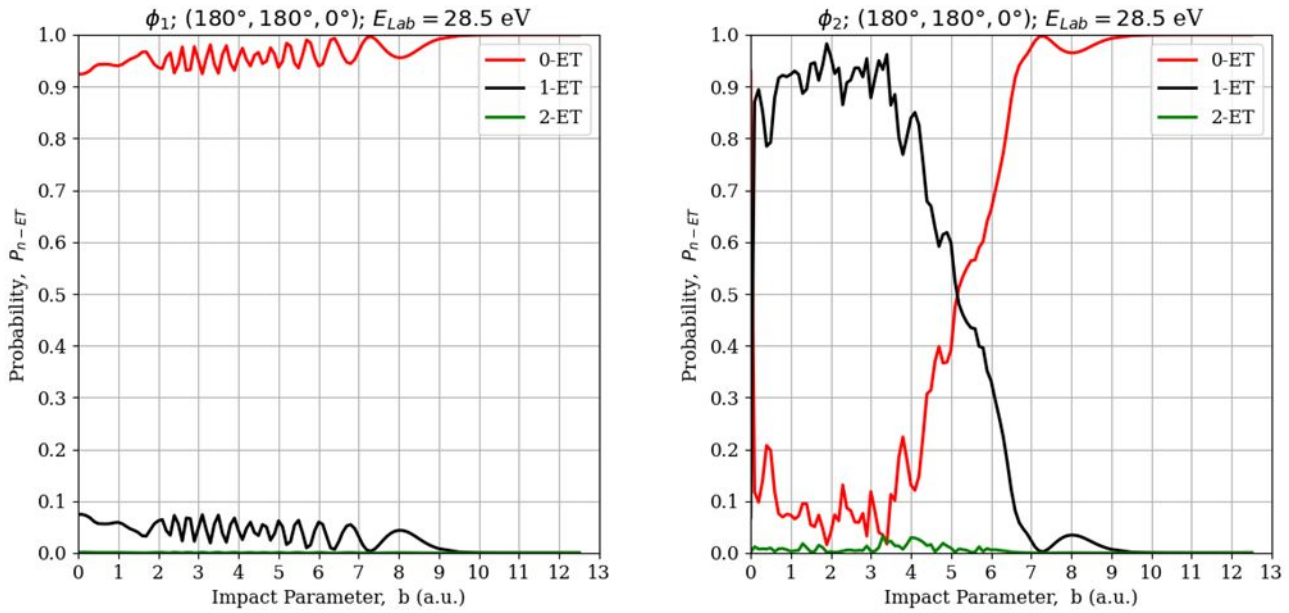

Figure 8: Projectile-to-target 0-, 1- and 2-electron-transfer (ET) probabilities P_{n_ET} vs. impact parameter b of SLEND/6-31G** simulations at E_{Lab} = 28.5 eV from projectile-target orientation (180°, 180°, 0°) and for symmetry-breaking parameters ϕ_1 (symmetry-preserving dynamics, left panel) and ϕ_2 (symmetry-breaking dynamics, right panel).

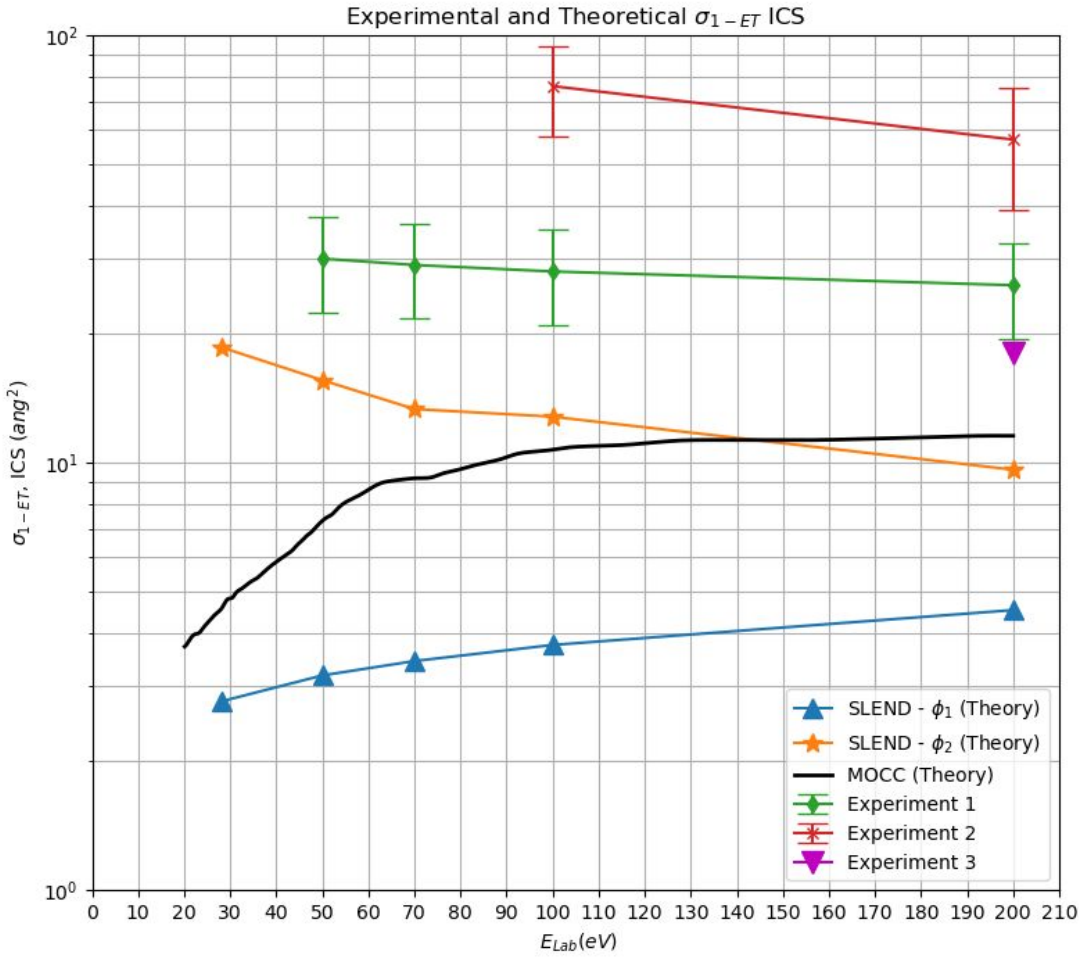

Figure 9: Projectile-to-target 1-electron-transfer (1-ET) integral cross sections (ICSs), $\boldsymbol{\sigma_{1-ET}}$, of $H^+ + H_2O$ vs. the collision energy E_{Lab}. Measured results from Experiment 1 by Barnett et al. (1977)[14], Experiment 2 by Coplan et al. (1970)[15], and Experiment 3 by Cable (1967)[16]. Theoretical results from SLEND/6-31G** simulations with symmetry-breaking parameter ϕ_1 (symmetry-preserving dynamics) and ϕ_2 (symmetry-breaking dynamics), and from molecular-orbit close-coupling (MOCC) calculations by Mada et al. (2007)[31].

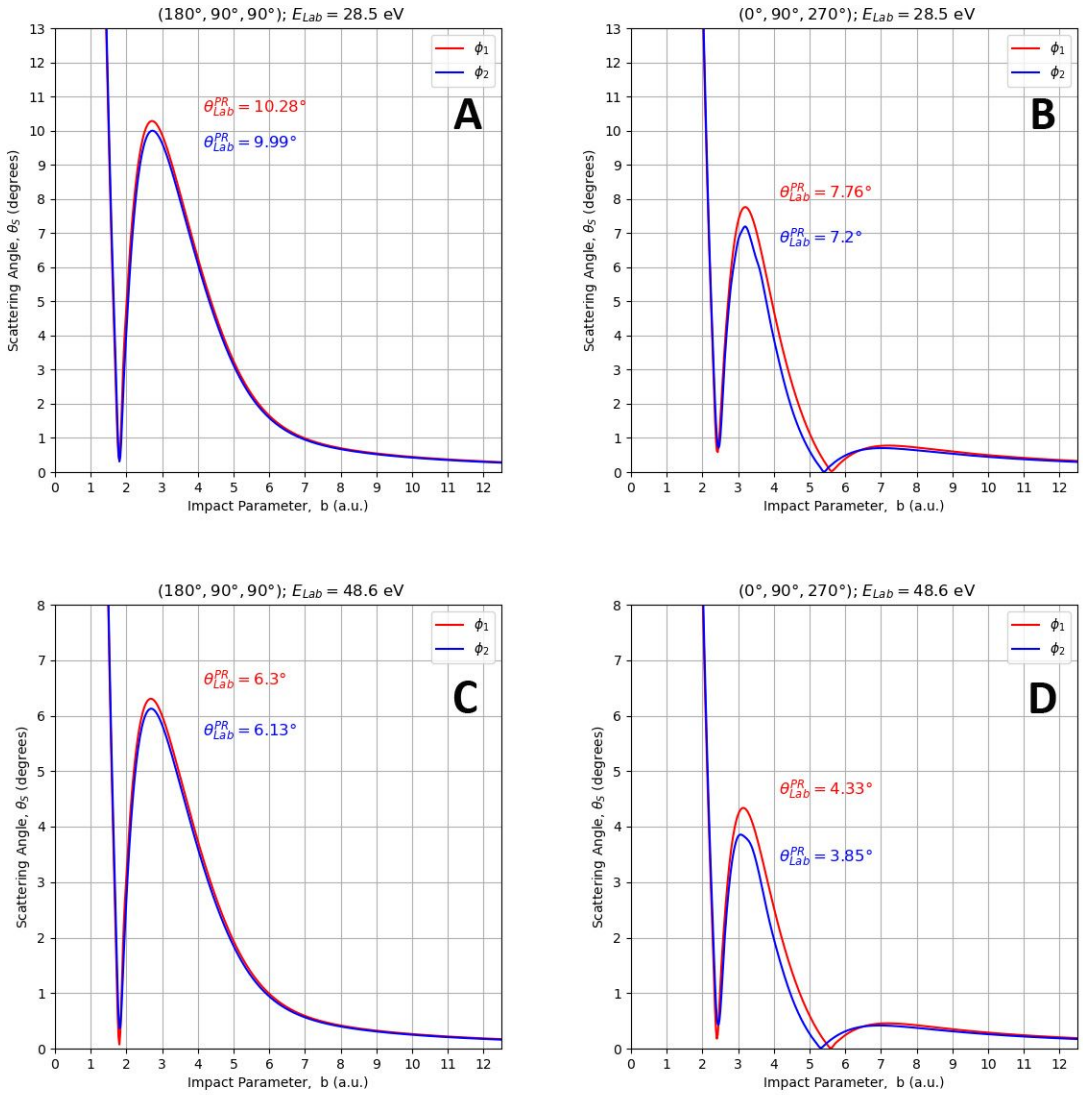

Figure 10: Classical projectile scattering angle functions $\theta_{Lab}(b)$ in the laboratory frame vs. impact parameter b of SLEND/6-31G** simulations of $H^+ + H_2O$ at energy $E_{Lab} = 28.5$ eV and projectile-target orientations (180°,90°,90°) (panel A) and (0°,90°,270°) (panel B), and at energy $E_{Lab} = 48.6$ eV from projectile-target orientations (180°,90°,90°) (panel C) and (0°,90°,270°) (panel D), and with symmetry-breaking parameters ϕ_1 (symmetry-preserving dynamics, red curves) and ϕ_2 (symmetry-breaking dynamics, blue curves). The tall maxima correspond to classical primary rainbow angles θ_{Lab}^{PR}.

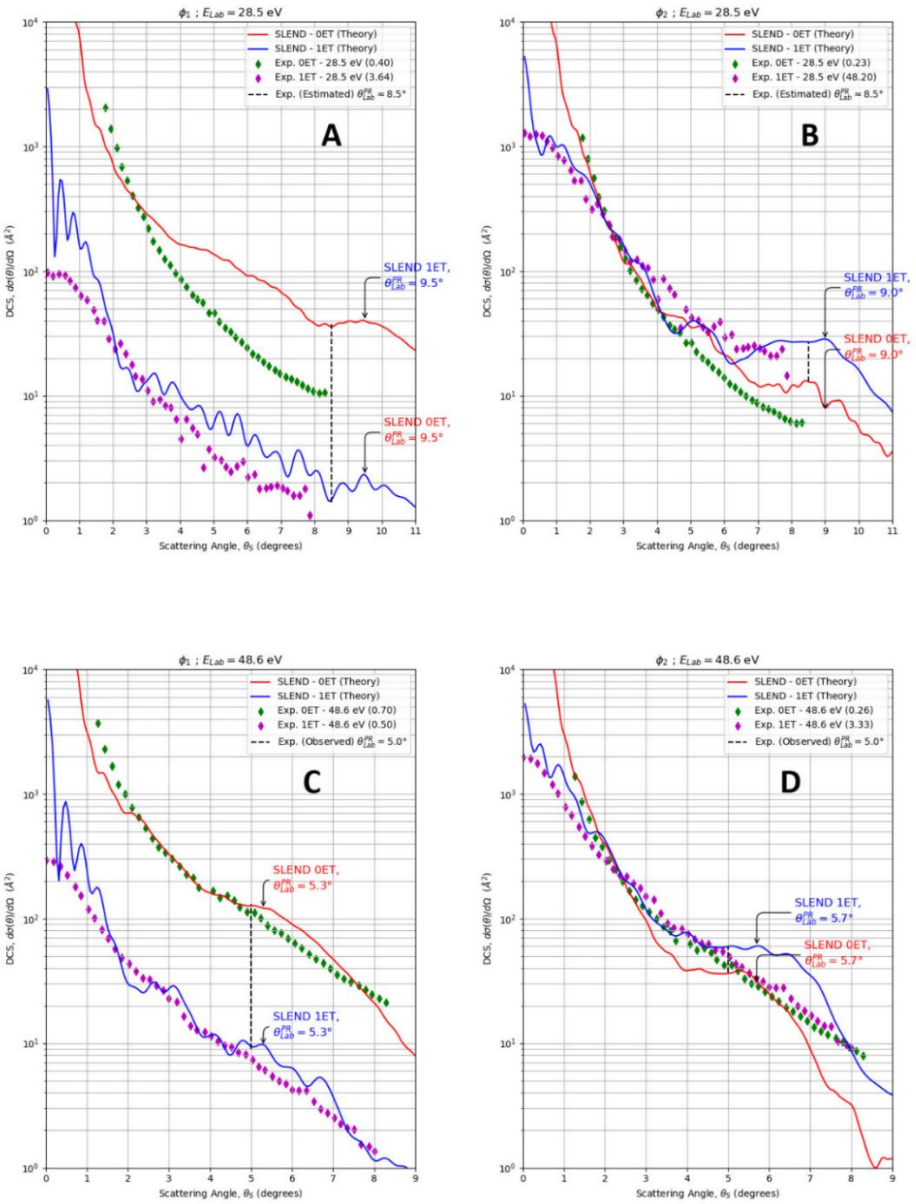

Figure 11: Projectile-to-target 0- and 1-electron-transfer (ET) differential cross sections (DCSs) of $H^+ + H_2O$ at $E_{Lab} = 28.5$ eV (panels A and B) and 48.6 eV (panels C and D) vs. the scattering angle θ in the laboratory frame. Experimental DCSs by the Toennies group (1987)[17] in comparison with their SLEND/6-31G** counterparts with symmetry-breaking parameter ϕ_1 (symmetry-preserving dynamics, panels A and C) and ϕ_2 (symmetry-breaking dynamics, panels B and D). In each panel, the experimental DCSs originally reported in relative units were normalized with respect to their SLEND counterparts (cf. Sect. 4.4 for details); normalization factors are given in the legends. For ϕ_1, the standard deviations of the 0- and 1-ET SLEND/6-31G** DCSs with respect to the normalized experimental data are 73.04 Å^2 and 3.45 Å^2 at $E_{Lab} = 28.5$ eV, and 22.39 Å^2 and 3.15 Å^2 at $E_{Lab} = 48.6$ eV, respectively. For ϕ_2 , those standard deviations are 8.93 Å^2 and 15.04 Å^2 at $E_{Lab} = 28.5$ eV, and 16.66 Å^2 and 21.63 Å^2 , at $E_{Lab} = 48.6$ eV,

respectively. Experimental and theoretical primary rainbow scattering angles are given in the legends and marked in the curves, respectively.